Chair of Physics

Master's Thesis

In-situ SAXS investigation of the evolution of hierarchical porosity of a soft carbon precursor during heat treatment

Max Valentin Rauscher, BSc

November 2022

MONTANUNIVERSITÄT LEOBEN
www.unileoben.ac.at

EIDESSTATTLICHE ERKLÄRUNG

Ich erkläre an Eides statt, dass ich diese Arbeit selbständig verfasst, andere als die angegebenen Quellen und Hilfsmittel nicht benutzt, und mich auch sonst keiner unerlaubten Hilfsmittel bedient habe.

Ich erkläre, dass ich die Richtlinien des Senats der Montanuniversität Leoben zu "Gute wissenschaftliche Praxis" gelesen, verstanden und befolgt habe.

Weiters erkläre ich, dass die elektronische und gedruckte Version der eingereichten wissenschaftlichen Abschlussarbeit formal und inhaltlich identisch sind.

Datum 16.11.2022

Unterschrift Verfasser/in
Max Valentin Rauscher

Acknowledgments

First of all, I would like to thank my supervisor Oskar Paris for giving me the opportunity to work on this thesis and for guiding me throughout the process. His untiring dedication to dig deeper has often led me to do extra work that I would have otherwise abandoned.

I would also like to thank Malina Seyffertitz for the interesting and enjoyable discussion of the scientific problems at hand. I am very grateful for your prior engagement with the material presented in this thesis and also for the help during the trip to ELETTRA.

I would like to thank Nicola Hüsing and Richard Kohns from Paris Lodron University Salzburg for providing the material studied in this work. The beam time at ELETTRA would not have been so productive without Richard's help. Not only did he take on most of the night shifts, but he also synthesised the material and helped me with the chemical issues that arose. I am very grateful to him for that.

I would like to thank Sebastian Stock and Nikolaos Kostoglou for introducing me to the gas adsorption measurements and for helping me with the data analysis.

Furthermore, I want to thank the people working at the Austrian SAXS beamline at ELETTRA and especially Heinz Amenitsch for the support during the experiments.

I would also like to thank my colleagues and friends at the Institute of Physics for the wonderful time and the interesting discussions. In particular, I would like to thank Rainer Lechner and Gerhard Popovski for the discussion, help and scientific input during my work.

Finally, I would like to thank my family and friends for their emotional support. Especially, I would like to thank my parents for giving me the opportunity to study full time at university. I would like to thank my sister Franziska Rauscher for her help and support. I am also very grateful for the patience and support from my partner Anna.

Abstract

Nanoporous carbons show versatile applications in various fields, such as electrochemical energy storage (e.g. supercapacitors), gas storage, and devices for water deionization. It was shown that electrochemical energy storage devices benefit from materials with hierarchical porosity. In this study, one such hierarchically structured carbon, namely soft templated carbon (STC) was investigated. The STC material presented in this work was provided and synthesized by the Paris Lodron University Salzburg. STC synthesis is based on the self-assembly of rod-like micelles on a two-dimensional hexagonal lattice, acting as a mesopore space template, surrounded by a polymer. During calcination (i.e. a temperature treatment in an oxidizing atmosphere at about 300 $°C$) the micelles are removed, resulting in a mesoporous polymer matrix which is subsequently carbonized and activated at temperatures >800 $°C$. This thesis aims to find optimized calcination parameters. This is done by time-resolved in-situ small-angle X-ray scattering (SAXS) of the STC material during calcination using synchrotron radiation. The influence of the variation of calcination temperature, time, ratio of nitrogen and oxygen in the atmosphere, and heating rate are studied. Structural changes are evaluated using multiple parameters derived from SAXS by a model-based approach. Adjusted calcination conditions are suggested for an optimized mesostructure of the resulting carbon precursor material. Additional gas adsorption analysis and thermogravimetric analysis are performed and presented in this work, contributing to a more complete understanding of the structural changes. This contributes to the improvement of the synthesis of STCs, and as a result, leads to optimized materials with application-relevant tailored pore properties.

Abstract

Nanoporöse Kohlenstoffe werden in verschiedenen Bereichen eingesetzt, darunter elektrochemische Energiespeicher (z.B. Superkondensatoren), Gasspeicher und zur Wasserentionisierung. Es wurde gezeigt, dass elektrochemische Energiespeicher von Materialien mit hierarchischer Porosität profitieren. In dieser Arbeit wurde ein solcher hierarchisch strukturierter Kohlenstoff aus einer Soft-Templating-Carbon-Route (STC) untersucht. Das in dieser Arbeit vorgestellte Material wurde von der Paris Lodron Universität Salzburg zur Verfügung gestellt und synthetisiert. Die STC-Synthese basiert auf der Selbstorganisation von stäbchenförmigen Mizellen auf einem zweidimensionalen hexagonalen Gitter, das als Vorlage für den Mesoporenraum dient und von einem Polymer umgeben ist. Bei der Kalzinierung (d.h. einer Temperaturbehandlung in einer oxidierenden Atmosphäre bei etwa 300 $°C$) werden die Mizellen entfernt, wodurch eine mesoporöse Polymermatrix entsteht, die anschließend bei Temperaturen >800 $°C$ karbonisiert und aktiviert wird. Die Suche nach idealen Kalzinierungsparametern erweist sich als schwierig. Hier präsentieren wir zeitaufgelöste in-situ-Kleinwinkel-Röntgenstreuung (SAXS) mit Synchrotronstrahlung des STC-Materials während der Kalzinierung. Der Einfluss der Variation der Kalzinierungstemperatur, der Zeit, des Verhältnisses von Stickstoff und Sauerstoff in der Atmosphäre und der Heizrate wird untersucht. Die strukturellen Veränderungen werden anhand mehrerer Parameter bewertet, die durch SAXS und einen modellbasierten Ansatz abgeleitet werden. Es werden optimierte Kalzinierungsbedingungen für eine verbesserte Mesostruktur des resultierenden Kohlenstoffmatrix vorgeschlagen. Zusätzliche Gasadsorptionsanalysen und thermogravimetrische Analysen werden in dieser Arbeit durchgeführt und vorgestellt und tragen zu einem umfassenderen Verständnis der strukturellen Veränderungen bei. Dies trägt zur Verbesserung der Synthese von STCs bei und führt zu optimierten Materialien mit anwendungsspezifischen Poreneigenschaften.

Abbreviations

STC	...	Soft Templated Carbon
$SAXS$	...	Small Angle X-ray Scattering
$EDLC$	...	Electric Double Layer Capacitor
OMC	...	Ordered Mesoporous Carbon
NCC	...	Nanocast Carbon
$IUPAC$	...	International Union of Pure and Applied Chemistry
MCM	...	Mobil Composition of Matter
MOF	...	Metal Organic Frameworks
COF	...	Covalent Organic Frameworks
PEO	...	Polyethylen Oxid
PPO	...	Polyphenylene Oxide
RF	...	Resorcinol Formaldehyde
TGA	...	Thermal Gravimetric Analysis
SEM	...	Scanning Electron Microscopy
TEM	...	Transmission Electron Microscopy
BET	...	Brunauer-Emmett-Teller
BJH	...	Barrett-Joyner-Halenda

Contents

1 Introduction

In the last century, porous carbons attracted the interest of many researchers, because of their outstanding combination of physical and chemical properties. The porous carbons referred to in this work are disordered, sp2 bounded carbons. Their main properties are the ability to have a high surface area, excellent thermal- and electrical conductivity and the ability to be produced by a large variety of sustainable sources at comparable low cost. Thus this material class can be used in various applications including energy storage devices (e.g. supercapacitors) [1–3], gas storage [4] and devices for water deionization [5, 6]. All these applications benefit from the high surface area making it one of the key selling points.

During the same period, more consideration and research on sustainability and environmental friendliness was done. Many attempts to produce existing technologies and devices sustainably have been conducted. One great example is the research in Electric Double Layer Capacitors (EDLC), using porous carbons as electrode materials [7]. It is possible, for example, to produce EDLCs with a water-based electrode (e.g. saltwater) in combination with activated carbon derived from coconut shells. The working principle of these devices is the formation of so-called electric double layers on the surface of the electrode. The ions in the electrolyte move to the electrode with the opposite charge polarizing the water and thus storing electricity. This process can be reversed and release energy [7, 8]. To increase its capacitance and ability for fast charging and discharging times (rate handling capability) research is conducted on these devices. Some reports suggest that high charging and discharging rates cause pores to be blocked. To reduce this phenomenon, increase rate handling capability and capacitance the use of Ordered Mesoporous Carbons (OMC) can be beneficial [2, 3, 9, 10].

The OMC presented in this work is a Soft Templated Carbon (STC), further detail in chapter 2, which consists of an ordered network of larger pores (2-50 nm), so-called mesopores, with unordered smaller pores ($<$2 nm), so-called micropores, in the bulk of the carbon.

1.1 Motivation

Research conducted by Koczwara in his thesis at the Institute of Physics in Leoben [3], investigating two OMCs, namely STCs and Nanocast Carbons (NCC)(more detail in chapter 2) indicate an increase in rate handling capability. STCs consist of rod-like mesopores arranged in a two-dimensional hexagonal lattice with micropores within the walls. The NCC are made up of interconnected two-dimensional hexagonal organized carbon rods containing micropores.

In that study, the NCC outperformed commercially available porous carbons and the STC as an EDLC electrode material. An important step for the fabrication of STC is calcination. It is a heat treatment under reducing atmosphere to remove the soft template, exposing the mesopores. Putz et al. [11] concluded that this heat treatment at 250 $°C$ may lead to insufficient removal. This means that some template material might be left inside the pores. In the following carbonization (heat treatment under inert atmosphere to convert carbon precursor material into carbon) the remaining template material might end up being carbonized as well as the surrounding carbon precursor. The resulting mesopores might be partially clogged or micropores are formed in the clogged areas.

The specific surface areas of the STCs investigated in Hasegawa et al. [12], calcinated at 300 $°C$, are considerable larger than in Koczwara et al. [2], calcinated at 250 $°C$. Combining the conclusion made by Putz et al. [11] and the difference in specific surface area lead to the assumption that the material used in Koczwara et al. [2] might have suffered from insufficient template removal and subsequently possibly blocked mesopores. For this reason, one might wonder how the comparison between a STC produced by optimized calcination and a NCC would have turned out in terms of the rate handling capability, surface area and capacity of an EDLC with carbon electrodes made from these materials.
This led to the interest and motivation to investigate the processes and the structural changes during calcination in hopes of finding optimized process parameters. Thermally treating STCs under enhanced conditions could generate materials with completely removed template while also preserving their hexagonal arrangement. Hopefully, this work leads to an increased surface area and improved electrode materials. In addition, this research could deepen the understanding of the processes during the calcination and results may be applied to the fabrication of this kind of material.

2 Nanoporous Materials

Researchers' interest in porous materials has experienced considerable growth over the last few decades. The earliest reports of porous material being used date back to 1500 BC. Ingestion of Egyptian ink was reportedly used as a medical practice. We know that the medical effect is a result of the porous charcoal inside the ink. Even nowadays charcoal tablets are administered to treat various gastrointestinal diseases such as food poisoning and nausea. Another porous material used as oral anti-diarrhea medicine is Kaolinite, a clay mineral. It was used throughout the world and was also for a long time the main ingredient for the commercially sold drug "Kaopectate" [13].

During the following centuries, various applications of charcoal are documented, for instance, ancient Hindu sources report the use of charcoal for purifying water [13, 14]. Many different porous solids have been found or produced, and combined with more sophisticated characterization methods down to the nanoscale, therefore a clear definition and clarification of these materials was needed.

This thesis follows the IUPAC recommendations [15] regarding the clarification mentioned above. In accordance with the IUPAC recommendations a porous solid, referred to in this work as porous material, is a solid with pores in the form of cavities, channels or interstices, which are deeper than they are wide. Additionally, following the same recommendations classifying these materials based on pore size, into microporous ($<2\ nm$), mesoporous (between 2 - 50 nm) and macroporous ($>50\ nm$) [14, 15]. This clarification can also be used to classify porous materials as presented in Figure 2.1. A different approach is a classification depending on the type of material making up the framework.

2.1 Overview of Porous Materials

Over the centuries many porous materials have been found and produced for various purposes, as can be seen in Figure 2.1. In this chapter a brief discussion of selected important porous solids is presented, to showcase the variety of porous materials and their different approaches to fabrication.

Zeolites are a material class that can be found in nature, although in industrial applications synthetic Zeolites are commonly used. These solids are crystalline aluminosilicates and have cavities in the range of 0.3-1.5 nm [16] and possess the ability to exchange cations due to the presence of a negative charge in the network. The framework is comprised of $SiO_4{}^{-4}$ and $AlO_4{}^{-5}$ arranged in tetrahedrons. For every silicon building block that is substituted by an aluminum node, one negative charge remains within the framework. Thus they can be used as water softeners, cracking catalysts and gas purification agents [16, 17].

In the 1980s Zeolites have become an industry standard but the research did not stop there. In the next decade, a new material class emerged: mesoporous materials. These types of materials can be composed of disordered and ordered mesopores. The later is especially interesting for this thesis. Its favorable properties include high surface area, the ability to tune the pore size and allow different pore shapes during synthesis [17]. Its fields of applications can range from catalysts to drug delivery. The most famous subclass is the ordered mesoporous silica. The so-called Mobil Composition of Matter (MCM) was the first synthesized variant. These MCMs employed the use of surfactants to generate ordered rod-like pores. The synthesis of such materials is based on the self-assembly of the template. This process is described in more detail in the next chapter. Another prominent example of these materials is the so-called SBA-15 type made with triblock copolymer as a template. The pores are rod-like and arranged in a hexagonal lattice, similar to MCM-41. Other possible arrangements of similar materials are the cubic and lamellar arrangement. The structure can be changed by varying the type of surfactant, the ratio between silica and template and the acidity of the solution [16–18].

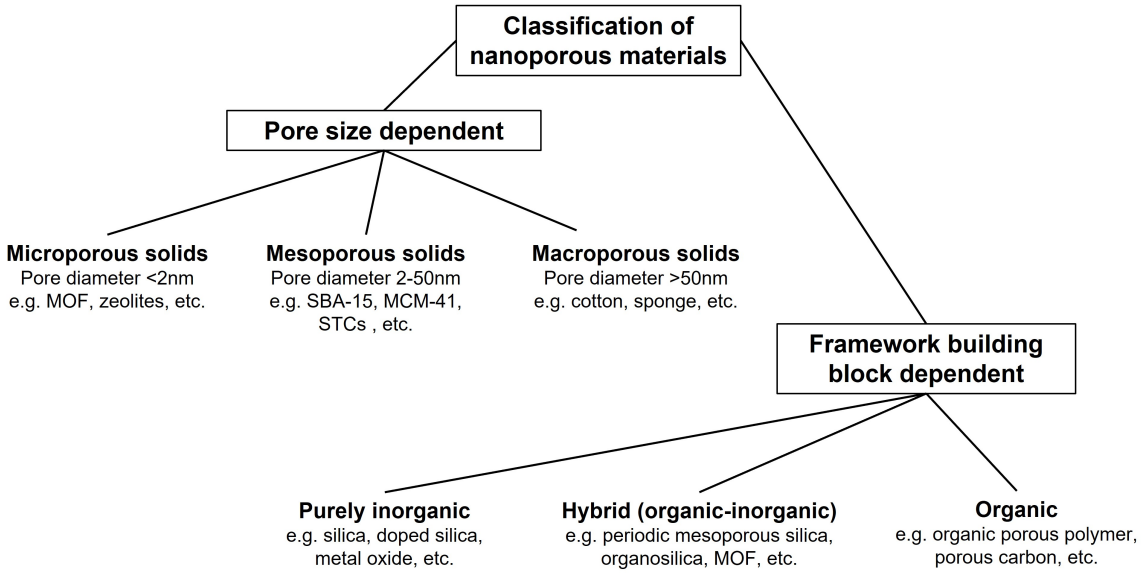

Figure 2.1: Flowchart of classification of mircoporous materials similar to [17]

All of the above described materials are purely inorganic. An example for organic-inorganic hybrid novel porous material is the class of Metal Organic Frameworks (MOF). The basic structure consists of metal ions or clusters that are interlinked with organic matter forming rigid networks with porosity. Today there are plenty of different MOFs with tailored pore sizes. This vast amount is due to the variety of possible metal ions and clusters that can be used as a base for the framework [16, 18].

An example of purely organic porous materials are Covalent Organic Frameworks (COF). They are crystalline in nature and often described as porous polymers. These materials consist of light elements (i.e. carbon, nitrogen, boron, etc.) that are bonded via strong covalent bonds. This class of materials is similar to MOFs in the sense that the pore structure can be easily tuned by changing the base of the network. An advantage compared to MOFs is that they possess higher chemical and thermal stability making them also available for post-synthesis processes [16, 18, 19]. The last porous materials highlighted in the next chapter are carbons.

2.2 Porous Carbons

Porous Carbons can be derived directly from natural products or synthesized with a tailored microstructure. They often have advantages in terms of sustainability and environmental friendliness. The porous carbons can be categorized into two groups the commercially available non ordered porous carbons and the ordered porous carbons. The former can be produced simply by the carbonization and, if needed, subsequent activation of source material. These source materials can be natural (coconut shell, wood, olive or peach pits, etc.) or synthetic (polymers) [20]. Carbonization is a thermal treatment of specimens in an inert atmosphere with temperatures ranging from 300-1500 $°C$ [21]. It is used to remove most of the volatile matter and to transform the source material into carbon with a similar structure to multilayer graphene.

Activation happens at elevated temperatures and is typically done in two different ways. The physical activation route requires carbonization prior to introducing a mild oxidizing agent (i.e. CO_2, steam, etc.) at temperatures between 800-1000 $°C$ [16]. Unlike physical activation, the chemical activation does not need carbonization beforehand. Mostly KOH and NaOH are introduced at temperatures between 250-650 $°C$ [16] to achieve the final structure. It consists of disordered pores of wide varied sizes. They can have a surface area up to 3000 m^2/g [22]. As mentioned in chapter 1.1 for some applications these commercially available porous carbons can be outperformed by ordered mesoporous carbons [16, 17, 20–22].

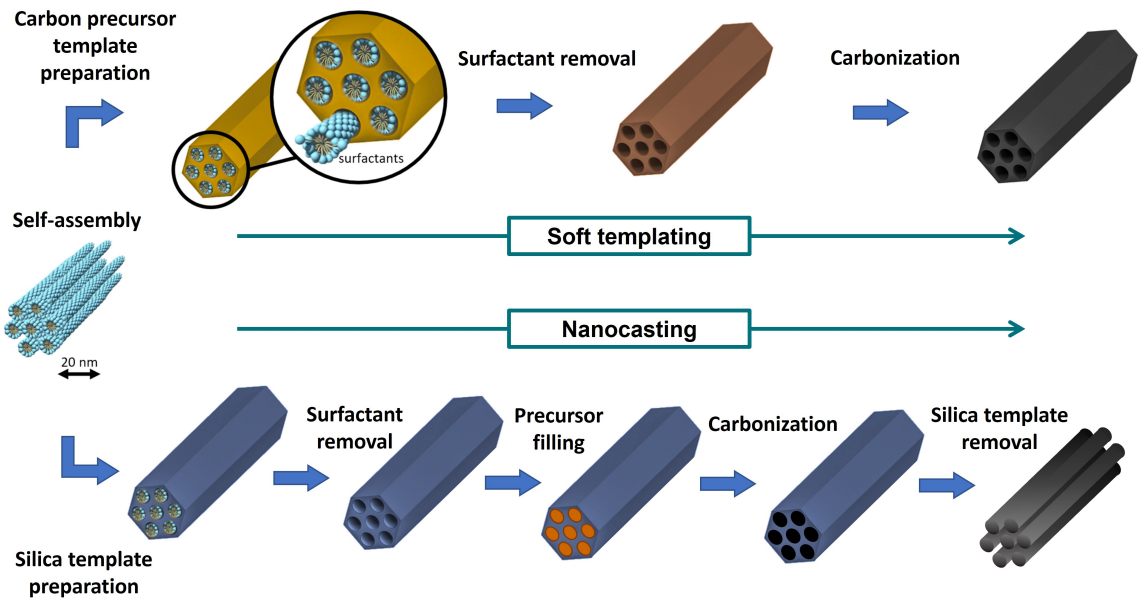

Figure 2.2: Schematic illustration of synthesis process for OMCs similar to [23]

The first reports of OMCs were published in 1999. In these reports a method was used called hard-templating or nanocasting. The name stems from the fact that mesoporous silica (e.g. SBA-15) is used as template for casting polymers. As can be seen in Figure 2.2, the ordered rod-like holes in the silica are filled with a carbon rich substance. This step is also referred to as nanocasting. In this condition, the polymer is carbonized and afterwards, the template is removed via a solvent, leaving the nanometer size rods. After the silica is removed the rods represent a negative of the template. As described, this approach requires a mesoporous silica template that has to be synthesized and heat-treated prior to being used. This process is not time efficient and requires HF or NaOH solutions, making the process neither resourceful nor environmentally friendly [16, 17, 21, 22].

2.2.1 Soft Templated Carbons

In search of a direct method to generate OMCs to counter the disadvantages of hard templating, a technique called soft-templating was developed. The process for these OMCs is similar to the creation of mesoporous silica. The schematic representation of this process can also be found in Figure 2.2. The first step in the fabrication is the creation of the template.

For this, surfactants possessing hydrophobic and hydrophilic groups within the molecules are needed. The following processes are described for triblock polymers (Pluronic) as Pluronic F127 is the template polymer used for the investigated material in this thesis.

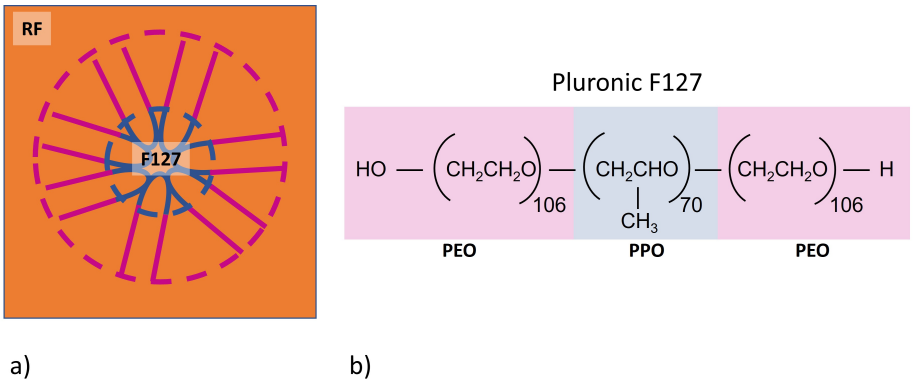

Figure 2.3: a) Schematic representation of the soft template (F127) surrounded by the carbon precursor (RF) b) chemical composition of F127

The base material F127 is dissolved under conditions that form liquid crystals due to its amphiphilic character. These conditions are called Critical Micelle Concentrations (CMC). The first CMC is the condition where spherical micelles are formed and the second CMC is required for the cylindrical (rod-like) micelle configuration. The material used in this thesis is made after a process described by Hasegawa et al. [12]. For this Pluronic F127 (PEO_{106} PPO_{70} PEO_{106}, schematic in Figure 2.3 b)) and resorcinol was added to a mixture of triethylene glycol, 1,3,5-trimethylbenzen, benzylalcohol and HCl in aqueous solution and stirred until complete dissolution. To this mixture, formaldehyde solution is added and again mixed in and kept at 60 $°C$ for 48 h. The Resorcinol Formaldehyde (RF) acts as the carbon precursor for the final structure. The concentration of the surfactant in the solvent must be above the second CMC in order to create the wanted configuration. The triblock copolymers arrange, due to self-assembly, into cylindrical micelles which in turn also assemble into a two-dimensional hexagonal lattice, visible in Figure 2.2. The gel is subsequently washed with H_20 and dried. In Figure 2.3 a) representation of the filled pore is given. After this processes, the polymeric framework is cured enough for the removal of the surfactants. It is typically heat-treated (calcinated) between 250-350 $°C$ for 0.5-2 h in oxygen containing atmosphere to remove the surfactants. The last step in order to generate STCs is to perform carbonization and if necessary activation, similar to regular carbons [12, 16–18].

3 Characterization Techniques and Analysis

Since the goal of this thesis is to optimize the calcination of a STC with Pluronic F127 surfactants, the changes at the nanometer scale during this heat treatment need to be investigated. Therefore, Small Angle X-ray Scattering (SAXS) is chosen as the main characterization technique for this thesis. In-situ experiments are performed at the synchrotron ELETTRA in Trieste over a period of 5 days. In these experiments, multiple process parameters are changed and their influence on the material measured. This initial study needed subsequent characterization techniques and experiments to contribute to their interpretation.

Thermal Gravimetric Analysis (TGA) and gas adsorption analysis are two analysis techniques performed to contribute to the evaluations and assumptions made with the in-situ experiments. The TGA is needed to measure the mass loss over time with varying process parameters. To correlate with the in-situ experiments, the samples are subjected to similar conditions.

Gas adsorption analysis is needed in order to conclude successful removal of F127 (i.e. creation of mesopores) and to generate structural information (e.g. pore size, surface area, etc.) complementary to the information generated with SAXS.

Additional structural information is obtained with Scanning Electron Microscopy (SEM) and Transmission Electron Microscopy (TEM). TEM images are acquired using a "Thermo Scientific Talos F200X G2 TEM" by Thomas Kremmer and provided by the "Lehrstuhl für Nichteisenmetallurgie" at Montanuniversität Leoben. SEM images are acquired using a "FE-SEM Tescan CLARA" by Gerhard Hawranek and provided by the "Lehrstuhl für Metallkunde und metallische Werkstoffe" at Montanuniversität Leoben. The resulting images in combination with Helium Pycnometry data generated at the "Institut für Chemie und Physik der Materialien" at the Paris Lodron University Salzburg are used as complementary information to characterize the material up to macroscale. The following chapter will provide the basic concepts and terms for understanding the main characterization techniques.

3.1 Small Angle X-Ray Scattering and Diffraction

This technique relays on the scattering of x-rays by matter and the detection of the resulting signal. Hence, for understanding the basics of this technique the first aspect to look at are the interactions of photons with matter. The electromagnetic waves can be absorbed, scattered, or no interaction can occur (transmission) within the specimen. In the case of absorption of an incident photon, the absorbed energy is either used to heat up the specimen or to remove an electron from an atom putting it in an excited state. In this state, it aspires to reduce its energy back to the ground state by getting rid of energy. This can be achieved by the emission of photons. It is called fluorescence radiation and is composed of x-rays with characteristic (atom dependent) radiation but different wavelengths than the incident beam. Absorption efficiency is dependent on the incident wavelength and the electron configuration of the material.

For transmission the direction of the wave does not change. In SAXS this part of the signal is called a direct beam. The beam size on the detector should be as low as possible in order to separate the transmission signal from very small scattering angles [24]. Scattering on the other hand can be described as a summation of two contributions. There is the coherent scattering contribution (i.e. Thompson scattering in the case of x-ray radiation). It occurs due to energy transfer between incoming photons with strongly bound electrons. These core electrons oscillate with the same frequency as the incident wave and can cause the emittance of radiation of electromagnetic waves sharing the same frequency. The oscillation of neighboring nuclei is synchronous, making the produced waves coherent.

The other contribution is the incoherent term. It is a result of Compton scattering where x-rays collide with electrons in the irradiated sample and change directions and lose energy (i.e. it now possesses a different frequency). Because of the random nature of the amount of energy loss, this term, unlike coherent scattering, does not provide access to structural information [24, 25].

Unlike transmission, scattering changes the direction of the beam. Viewing the material in an atomistic manner, every particle can act as a scattering center (i.e. emitting an electromagnetic wave).

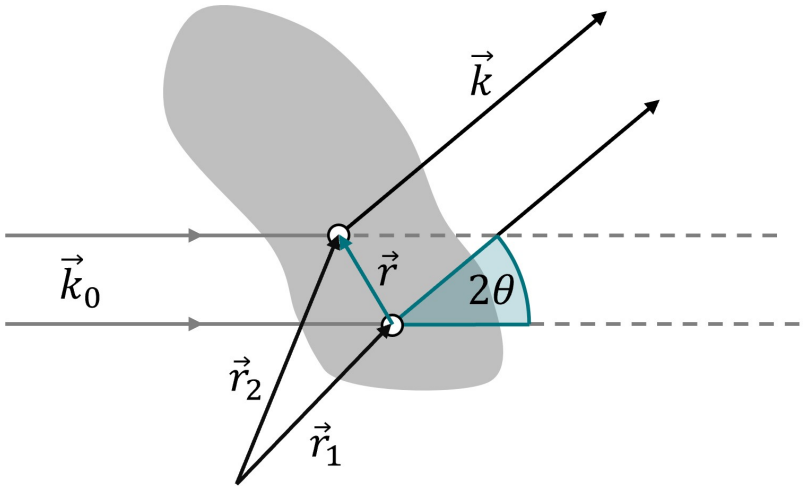

Figure 3.1: Schematic representation of scattering and the relations between the beams

For coherent scattering the energy is conserved but a change in momentum occurs. This change can be expressed as [26]:

$$\hbar\vec{q} = \hbar * (\vec{k} - \vec{k_0}) \tag{3.1}$$

$\hbar$	...	*planks constant*
$\vec{k}$	...	*scattered wave vector*
$\vec{k_0}$	...	*incident wave vector*
$\vec{q}$	...	*scattering vector*

The difference between the outgoing and incoming wave vectors is then defined as the scattering vector $\vec{q}$. Any spherical wave emitted from a scattering centre can be treated as a plain wave in the far field. In Figure 3.1 the relations of the wave vectors are depicted. The coherent scattered plain waves can interfere with each other depending on their respective phase difference. If it is equal to even multiples of π (2π, 4π,...) constructive interference and for odd multiples destructive interference occurs [24–26] .
The phase difference can be described with [26]:

$$\Delta\phi = \vec{r} * \vec{q} \tag{3.2}$$

where:

$\Delta\phi$	...	*phase difference*
$\vec{r}$	...	*distance between scattering centers*

For elastic scattering where $|k_0| = |k|$ the scattering vector length q can also be written as [26]:

$$q = |\vec{q}| = \frac{4\pi}{\lambda} \sin \Theta \tag{3.3}$$

where:

λ ... *wavelength*
2Θ ... *scattering angle*

With this Equation, the detected scattering profile can now be represented as a function of scattering vector length (q) rather than scattering angle, as is done in this thesis.

Let us now consider the scattering on one particle of specific shape. It is made out of multiple atoms and possesses an ensemble of scattering centers (i.e. electrons) that produce scattered waves. These waves can interact with each other according to the Equation 3.2, resulting in an detectable interference pattern. It is the square of the sum of all scattering wave amplitudes dependent on the scattering vector. This pattern is also called form factor $|F(q)|^2$ as it is characteristic to the particle's form [24–26].

For diluted particles it can be described in a general way as:

$$|F(\vec{q})|^2 = |\int\limits_{V_{particle}} \rho(\vec{r}) e^{i\vec{q}\vec{r}} d^3r|^2 \tag{3.4}$$

where:

$F(\vec{q})$ ... *scattering amplitude*
$\rho(\vec{r})$ ... *electron density*
$\vec{r_j}$ ... *position of scattering centers*

This factor must be scaled to the scattering profile with a constant to match the experimental intensities. In typical experiments, the irradiated particles often do not have the same shape and size, so the pattern obtained corresponds to the average over all individual form factors. If the particles are not diluted and the distances between them are in the same order of magnitude as their respective size another contribution to the scattering signal needs to be taken into account. It is called the structure factor $S(q)$ and contains an additional interference pattern that originates from the contributions of neighboring particles. It is multiplied in a simple approximation by the form factor to generate the scattering intensity.

This resulting accumulation of the individual scattering signals is called diffraction. For high orientation or alignment of the particles, distinct peaks (Bragg peaks) can be visible in the profile, as can be seen in Figure 3.2. The position of the peak maximum (q_{Peak}) can be used to calculate the distance (d_{Bragg}) between the particles [24, 25, 27].

Combining Equation 3.2 for the first constructive interference ($\Delta\phi = 2\pi$) and Equation 3.3 yields Bragg's Law described with the scattering vector [26]:

$$q_{Peak} = \frac{2\pi}{d_{Bragg}} \tag{3.5}$$

For a two-dimensional hexagonal lattice, like the material presented in this work, the scattering vector lengths of the Bragg Peaks can be calculated in a variation of Equation 3.1 as follows, if the lattice constant a is known [28]:

$$q_{hk} = \frac{4\pi}{a\sqrt{3}}\sqrt{h^2 + k^2 + hk} \tag{3.6}$$

where:

a	...	*lattice constant*
h, k	...	*miller indices for the lattice planes*
q_{hk}	...	q_{Peaks} *for each hk*

This summarises the basics of scattering. The following chapters are dedicated to the specific methods and models used to analyse the SAXS data presented in this thesis.

3.1.1 Analysis of SAXS profiles

This chapter will explain the analytical methods for analyzing the SAXS profiles in this thesis. The first step is to transform the signals recorded on a 2D detector into 1D scattering profiles. The data is averaged azimuthal in a q range of 0.2 to 9 nm^{-1} to generate spherical averaged intensity values $I(q)$. The scattering length is calculated according to Equation 3.3 with the characteristic wavelength of the incident beam (for the in-situ measurements it is 1.54 Å).

The typical scattering profile from STCs, as described in the previous chapter, is expected to have multiple sharp Braggs peaks due to the ordered arrangement of the soft template. In Figure 3.2 b) a typical scattering profile from STCs as well as a schematic of the hexagonal arrangement of triblock copolymers is depicted. In the later, the two smallest characteristic distances (d_{10}, d_{11}) between the ordered particles are represented and indexed with miller indices.

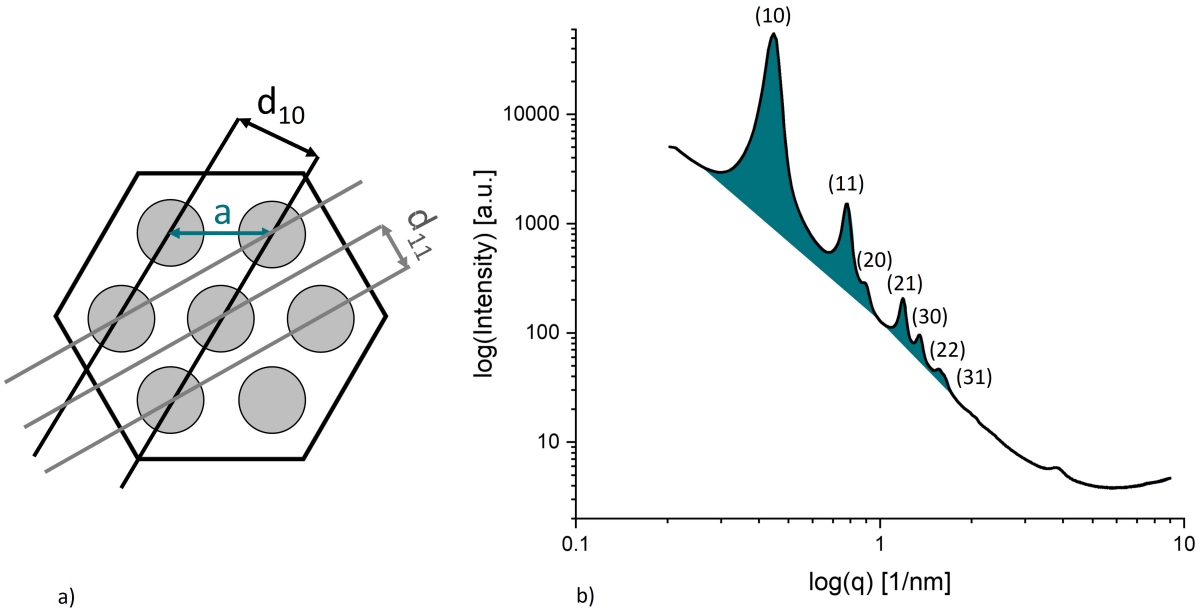

Figure 3.2: a) Schematic representation of the STCs structure with characteristic distances (d_{10}, d_{11}) and lattice constant (a) visualized, b) representative SAXS profile from uncalcinated STCs with highlighted Bragg peaks and $\tilde{I}_{Bragg}$

The Bragg peaks are clearly visible in the scattering profile. To confirm that these peaks correspond to a two-dimensional hexagonal arrangement the q_{Peak} values of each peak can be used to calculate the characteristic lattice constant a. In order to calculate the peak positions of each maximum the peaks need to be fitted. After they are fitted and peak positions are known the calculation confirms that the triblock polymers are arranged in this type of lattice. It is possible to separate the SAXS profile into two intensity contributions, the contribution from the diffraction on the hexagonal lattice I_{Bragg} and the diffuse scattering due to heterogeneities within the matrix and disordered pores I_{diff} [29].

Another analytical step taken is to calculate the integrated intensities $\tilde{I}$ according to [2]:

$$\tilde{I} = \int_0^\infty I(q) q^2 dq \tag{3.7}$$

$\tilde{I}$ is calculated for the entire scattering curve. This calculation is also done for each individual fitted peak without the background and the sum of these values is the integrated Bragg intensity ($\tilde{I}_{Bragg}$). The integrated diffuse intensity ($\tilde{I}_{diff}$) is the difference between $\tilde{I}$ and $\tilde{I}_{Bragg}$. Splitting the SAXS profiles into two contributions allows us to estimate the changes of the structure independently of the changes within the matrix. In Figure 3.2 the area under the peaks corresponds to $\tilde{I}_{Bragg}$.

According to Porod [30], in an ideal two-phase system, the slope of the scattering curve at high q values should be a power law with slope of -4 for sharp interfaces. This characteristic region is called Porod region. For the STCs in this work, this region is evaluated in the range of 2.3-7 nm^{-1}. In this regime, data are fitted with the following Equation [24, 31]:

$$I(q) = \frac{P}{q^{\alpha}} + C \tag{3.8}$$

where:

P ... *Porod constant*
α ... *exponent*
C ... *Constant*

For α values of 4 Equation 3.1.1 reduces to Porod's Law for sharp interfaces. If it is smaller than 4 it indicates a non sharp interface [30, 31].

3.1.2 Form Factor Models

The overall intensity can be described as mentioned in the previous chapter with the contribution of the form factor and the structure factor.
It can be written as [2]:

$$I(q) = KS(q)|F(q)|^2 \tag{3.9}$$

where:

K ... *Constant*

The structure factor for a two-dimensional hexagonal lattice can be written as [2]:

$$S(q) = \frac{1}{q^2} \sum_{hk} M_{hk} S_{hk}(q) \tag{3.10}$$

where:

M_{hk} ... *multiplicity factor*
S_{hk} ... *delta function at position q*

This is true assuming a spherical averaged structure. The multiplicity takes into account all possible lattice orientations that yield the same scattering vector. For the two-dimensional hexagonal lattice the multiplicity is 6 for all (h0) and (hh) Miller indices and 12 for all mixed (hk) indices [25]. Only in an ideal two-dimensional hexagonal lattice (i.e. perfectly ordered punctiform particles with no spatial extension) the Bragg peaks are delta functions.

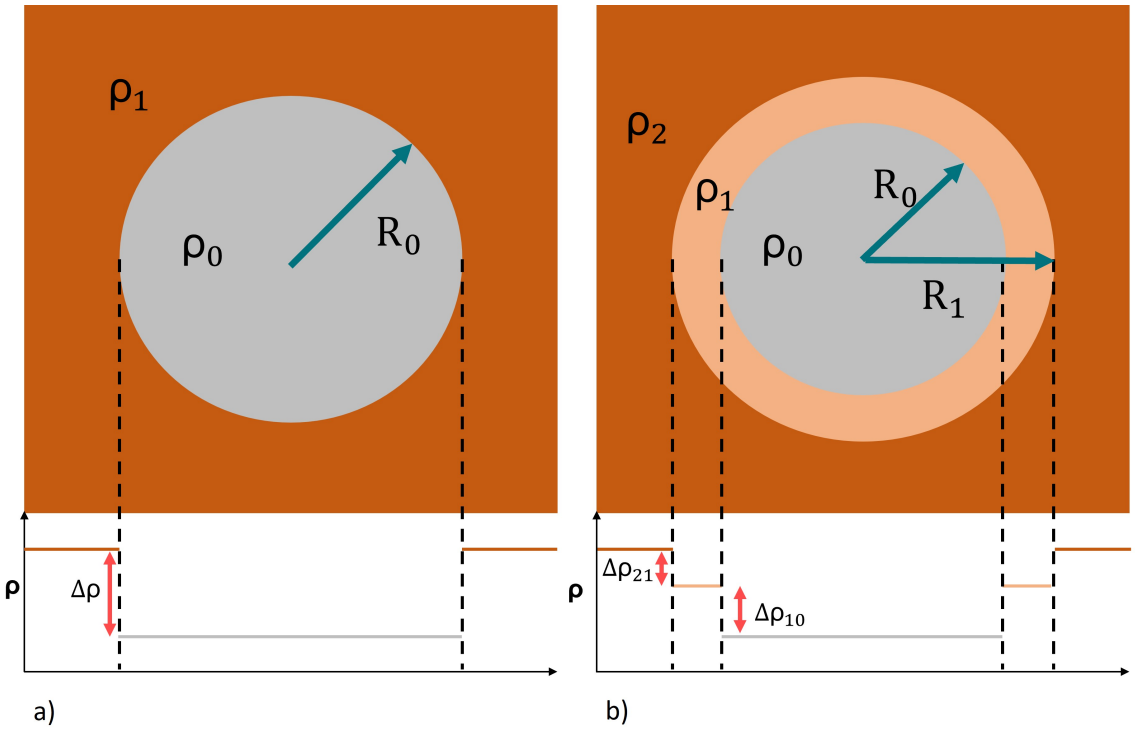

Figure 3.3: Schematic representation of the a) one-step- and b) two-step form factor model

In the real world Bragg peaks do not correspond to the ideal assumption of delta functions as particle volumes, irregular particles shapes and spacing as well as finite crystallite sizes lead to a broadening Bragg reflexes.

Following the model-based approaches of Impéror-Clerc et al. [32] and the subsequent work done by Zickler et al. [28] a model with one and two steps is constructed to generate a form factor which can be fitted to the data. The models are depicted in Figure 3.3, with ρ_i (i=0,1,2) as the individual electron densities, $\Delta\rho_{jl}$ as the difference in electron density ($\rho_j - \rho_l$ with j,l=0,1,2) at the interface and R_i (i=0,1,2) being the radii. For the single step model in Figure 3.3 a) only one radius R and one difference in electron density $\Delta\rho$ is used.

In both model approaches, the structure is considered to be perfectly ordered, i.e. the rod-like micelles and pores are located on the positions corresponding to a two-dimensional hexagonal lattice. Furthermore, the rod-like micelles and resulting pores are considered to be uniform in size with a circular cross-section and density. For the models, it is assumed that the length of each cylinder is much larger than the radii. Thus simplifications described in Pedersen [33] for such cases can be applied to the cylindrical models.

For the two-step model with this cylinder-cylinder shell combination the model is constructed in analogy to the spherical shell model described in Pedersen [33] resulting in:

$$F(q) = \frac{\Delta\rho_{10} R_0^2 \frac{2J_1(qR_0)}{qR_0} + \Delta\rho_{21} R_1^2 \frac{2J_1(qR_1)}{qR_1}}{\Delta\rho_{10} R_0^2 + \Delta\rho_{21} R_1^2} \tag{3.11}$$

with J_1 as the Bessel function of the first kind and first order.
For the one-step model it can be written as:

$$F(q) = \frac{2J_1(qR)}{qR} \tag{3.12}$$

Both models are fitted to the $\tilde{I}_{Bragg}(q_{hk})$ values of each peak. It is done by minimizing the difference for each peak which can be expressed as:

$$\frac{\tilde{I}_{Bragg}(q_{hk})}{M_{hk}} - (S(q)K|F_{Model}(q)|^2) \tag{3.13}$$

At this point, it is mentioned that this model can be further modified. For example, a Debye-Waller factor can be introduced in order to take static or thermal lattice distortions into account. A size distribution for the radii can also be introduced [28, 33, 34]. However, these complications are not considered in this work, as the data can already be described well without them.

3.2 Gas Adsorption Analysis

This technique is chosen to complement findings obtained from SAXS. It is possible to characterize the pore size (starting from 0.35 nm up to $\approx$ 100 nm) and the specific surface of porous materials [35].

For gas adsorption experiments, gas (adsorptive) is adsorbed by a solid (adsorbent). Adsorption is the accumulation of gas at the solid-gas interface. In the adsorbed condition the fluid is called adsorbate.

During measurements at constant temperature, the mass of adsorbed gas on the surface of a solid of known mass is recorded. At isothermal conditions this process is dependent on pressure and the interaction potential between adsorptive and adsorbent. A graph of the adsorbed mass at a given pressure is known as the adsorption isotherm.
The effect of adsorption can be categorized into physical- (physorption) and chemical adsorption (chemisorption). The first is a reversible process and generally occurs when an adsorptive is in contact with a solid surface.

During physorption no structural changes occur and multiple adsorbate layers may be formed. These characteristics make this effect suitable for surface area determinations [35].

Chemisorption, on the other hand, is irreversible and leads to structural changes. The gas is incorporated in chemical bonds at the surface. The adsorption is restricted to a single surface layer. Additionally, the adsorbed particles are more localized compared to physorption [35].

Analyzing the adsorption isotherms different distinct shapes can be characterized. The IPUAC recommendations [15] distinguish six different types. The type IV is typically found for mesoporous materials and represents the behavior of the isotherms measured with STCs (representative type IV adsorption isotherms can be found in Figure 6.12b)). They feature a hysteresis loop between the adsorption and desorption branches. Another distinct feature is the formation of a plateau at high relative gas pressures, indicating complete pore filling [35].

3.2.1 Surface Area and Pore Size Determination

Different methods for different materials have been developed over the past century. In this chapter only the methods important for this thesis are discussed. The Brunauer-Emmett-Teller (BET) [15] method is used for surface area evaluations. It can be used for materials generating type II and IV isotherms, as described in the IUPAC recommendations [15]. For the evaluation two steps need to be taken. Firstly, the physorption isotherm needs to be plotted as a BET plot. Relative pressure $p_{rel} = p/p_0$ is on the abscissa and on the ordinate is $p_{rel}/(n * (1 - p_{rel}))$, with n as the monolayer capacity (i.e. the volume of gas adsorbed at standard temperature and pressure). With this representation the BET monolayer capacity can be evaluated by the use of linear relation in such a representation. Secondly, the accessible BET derived area is calculated as follows [35]:

$$S_{BET} = \frac{nN_A\sigma_m}{m} \tag{3.14}$$

where:

S_{BET}	...	*BET specific surface area*
N_A	...	*Avogadro's constant*
σ_m	...	*molecular cross-sectional area*
m	...	*absorbent mass*

This evaluation is widely used and additional information can be widely found [15, 35].

The range between the p_{rel} values of 0.05-0.30 is called BET range. This range is used for the above described evaluation. In case of type IV desorption isotherms, pore condensation effects at low relative pressures need to considered when used for this surface area evaluation. If the characteristic hysteresis loop described for type IV isotherms does not close, (e.g. for the uncalcinated condition of the STC precursor presented in Figure 6.9), only the adsorption branch is used for the BET area calculation [15, 35].

For the mesopore size evaluation the Barrett, Joyner and Halenda (BJH) method is often used for mesoporous materials, under the assumption of cylindrical pores and that the adsorption is a result of physorption on pore walls and capillary condensation within mesopores. As many other methods it uses the modified Kelvin Equation [35]. Additional information can be found in Literature [15, 35, 36].

4 Experiments and Setups

The in-situ small angle x-ray scattering experiments are performed using synchrotron radiation at the Austrian SAXS beamline at ELETTRA in Trieste, Italy. At the Institute of Physics in Leoben additional ex-situ SAXS and gas adsorption measurements are performed. TGA measurements and sample preparations for gas adsorption are done at the Institute for Physics and Chemistry of Materials at the Paris Lodron University in Salzburg.

4.1 Synchrotron Experiment

4.1.1 In-situ Furnace

The furnace used for the in-situ experiments is depicted in Figure 4.1 a). The furnace can operate in a temperature range between 25-450 $°C$. It is composed of the heating unit, Figure 4.1 a)2), and a water-cooled base, Figure 4.1 a)1). The water-cooled base has two connections on one side to which the coolant tubes are attached. On the other side a screw is located to move the furnace vertically up an down. If the furnace is at the bottom end it is in direct contact with the base leading to insufficient heating.

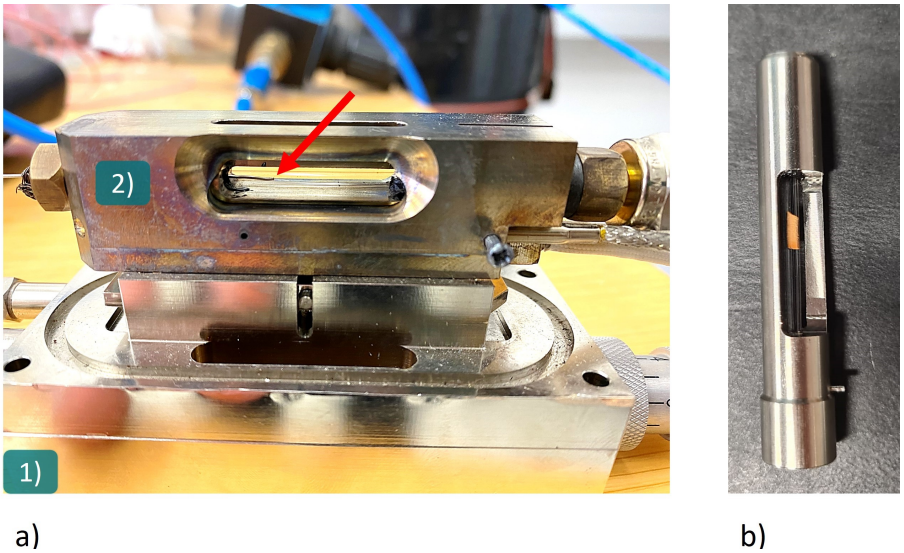

Figure 4.1: a) Image of the in-situ furnace (1) water-cooled base, 2) heating unit), b) sample holder with inserted sample, red arrow indicating the position of the thermocouple

The heating unit consists of a steel frame with windows for the passage of x-rays, an electric heating element inserted directly into the frame which is fastened with a screw (visible on the right side of the frame in Figure 4.1), and a thermocouple that is glued into the frame. The thermocouple and heating element are connected to a PID controller to set and control heating rates and temperatures. The sample holder depicted in Figure 4.1 b) is a cylindrical tube with a 3 mm through hole. In this hole a custom glass capillary is glued with heat resisting silicone. The capillaries used are of 1.5 mm diameter in the middle area but can be wider on the ends. Thus the through hole is larger to accommodate the varying widths. The capillary is glued into the holes with heat-resistant silicone to achieve an airtight seal. The sample holder can be inserted into the heating unit for measurements and pulled out again afterwards for loading and unloading sample material. When the sample holder is inserted a gas-connector on one side and a screw with a through hole is screwed on the other side. This hole is used to insert and hold another thermocouple to record the temperature during a measurement. The fully assembled furnace is depicted in Figure 4.2. The connected coolant tubes are visible in Figure 4.2(2) and the gas-connector in Figure 4.2(1).

At the beginning of each measurement, the sample holder is measured without a sample but with gas flow. Afterwards, it is filled with sample material, that is prepared from a monolith using a so-called biopsy punch.

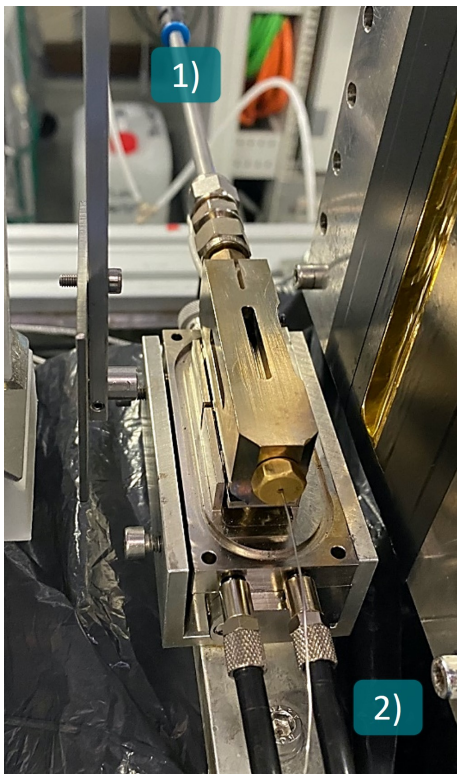

Figure 4.2: Assembled in-situ furnace at ELETTRA (1)gas-connector, 2)connected coolant tubes

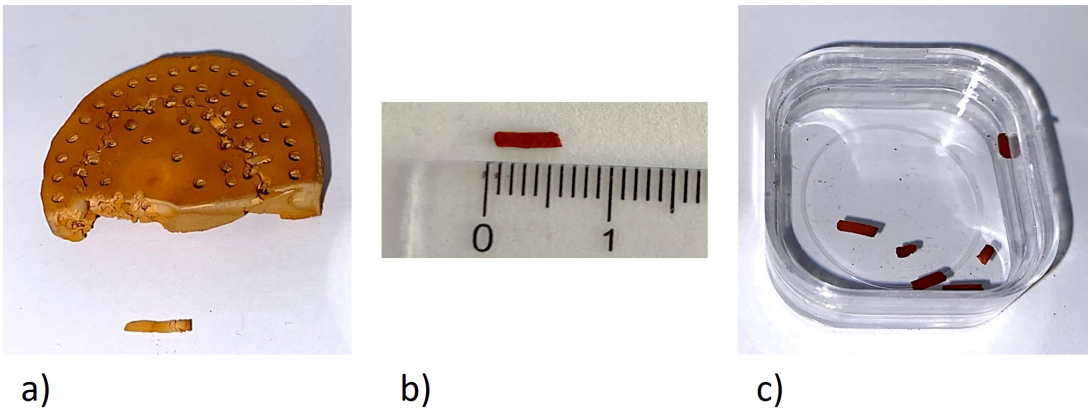

Figure 4.3: a) uncalcinated STC monolith with holes from punched out sample, b) punched out sample with dimensions, c) calcinated samples

A biopsy punch is a sharp round steel blade to remove skin for biopsy. This device additionally also very well suited for punching out cylindrical samples from the monolith, as shown in Figure 4.3. The cylindrical sample is then carefully inserted into the capillary inside the sample holder. During filling and handling of the sample holder, a toothpick is temporarily inserted at the other end to prevent the sample from falling out. When the sample is successfully inserted the toothpick is removed. Then the sample holder is inserted into the heating unit and the gas connection pipe and screw are tightened. The thermocouple is carefully inserted into the hole without damaging the capillary. With the thermocouple it is possible to move the sample inside the capillary (see the red arrow in Figure 4.1a)). The thermocouple held the sample material in place as it would have been pushed to one side by the gas flow.

4.1.2 Experimental procedure

The need for synchrotron radiation stems from the nature of time-resolved in-situ measurements. To obtain satisfactory statistics a higher flux compared to lab devices is needed. The monochromator at the beamline is set to 8.05 keV (wavelength 1.54 Å), the distance between the sample and the detector (2D Pilatus3 1M Detector System) is set to 758.4 mm and the beam size at the sample is 0.3x2 mm.

During furnace operation, a constant gas flow is applied with a flow rate between 0.5-1 L/min. The gas is a mixture of nitrogen gas and synthetic air (oxygen content of 21 %) and can be tuned to obtain different O_2 contents. For recording the temperature with the inserted thermocouple touching the sample a thermologger is used, that does not support the N-type thermocouples, which are needed in order to be inserted into the tube. The logger is set by default to measure with K-type thermocouple but only an N-type is available, thus resulting in inaccurate temperature readings.

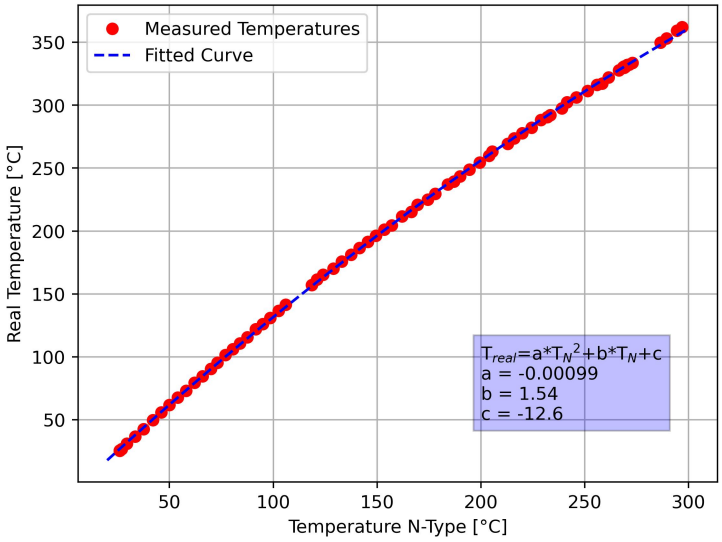

Figure 4.4: Calibration Curve for the thermocouple temperature correction

This problem is solved by performing a temperature calibration. A second thermocouple connected to a multimeter is put inside the tube on the opposite side so that both devices touched in the middle of the capillary, while no sample or gas flow is present. During a heating cycle to a maximum temperature, multiple measurements are done at the same time resulting in the calibration curve seen in Figure 4.4. This curve is then fitted with a second order polynomial and the optimized polynomial is subsequently used to calculate the real temperature. The errors of both thermocouples are ± 1 $°C$ or 0.75 % in the worst case for 350 $°C$ this results in a an error of ± 2.6 $°C$. The standard error of regression is 1.28 $°C$. Depending on the position of the sample in the capillary, the sample temperature can deviate by about 2-4 $°C$ over the length of a typical sample. Using this insight, the error of the recorded temperature is estimated to be around ± 3 $°C$.

Each experiment is subjected to controlled heating with a specific heating rate under gas flow. Upon reaching the desired temperature the oven is held at that temperature for a longer period of time, followed by a cool-down of the oven with the same gas flow as the holding period.

Multiple measurements are performed in a temperature range between 250-340 $°C$, with oxygen atmospheres of 2 and 10 % O_2 and with heating rates of 1, 3 and 10 $°C/min$. In order to better understand the processes several samples are heated under an inert N_2 atmosphere and oxygen is injected only after reaching a constant temperature.

Ex-situ measurements are performed with the instrument Nanostar (Bruker AXS). It is operated with a x-ray source at 45 keV and 0.65 mA, delivering CuKα of wavelength 1.54Å. The 2D SAXS signal is detected with a Vantec 2000 area detector.

4.2 Gas Adsorption

The samples in calcinated condition (approximately 100 mg) are degassed at 125 $°C$ under vacuum for 24 h (except for *HT 300 °C 120 min*, are only about 20 mg is available). The carbonised samples (approximately 50 mg) are degassed at 250 $°C$ under vacuum for 24 h. This is done to ensure that no physorbed species are present at the surface.

The sample material is placed in a 6 mm glass cylinder cell. To reduce the volume a glass filling rod is placed inside. The gas adsorption measurements are performed on a Autosorb-iQ3 (Anton Paar QuantaTec) gas sorption analyzer, at 77 K cooled by means of a liquid nitrogen filled vessel. N_2 of ultra high purity (99.999 %) is used as an adsorptive. The BET specific surface area and the BJH evaluation is performed with the program ASiQwin (version 5.21, Quantachrome Instruments).

4.3 Thermogravimetric Analysis

The thermogravimetric analysis is performed with a "Netzsch STA 449 F3 Jupiter". The device and sample loading procedure are displayed in Figure 4.5. The cylindrical pot used, had an inner diameter of about 0.5 cm and a depth of 1 cm. The analysis is done with a sample mass between 20-45 mg. In order to compare the TGA measurements to in-situ data selected heating rates and gas flow conditions are mimicked. It is important to note that even though the same parameters (heating rate, temperature, oxygen content) are used, the gas flow around the sample cannot be mimicked. In the TGA device, the air surrounds the sample material unlike the in-situ experiment where the gas can flow around and through the sample. The TGA is not only used as an analytical tool but also as a means to produce sample material, since there is no other suitable furnace available to produce the in-situ conditions as good as possible.

Figure 4.5: TGA setup and filling of ceramic pot

5 Evaluation of the In-situ Data

The data analysis steps described in the previous chapter need to be performed on every individual data set within one in-situ heat treatment. Each measurement consists of 250-1000 individual SAXS profiles. This large amount of data cannot be fitted and analyzed individually, promoting the need for computer automated fitting. A custom Python script is developed and the main programming steps and methods are described in the following paragraphs.

5.1 Porod Slope and Fitting Peaks

The first step the custom script carries out, is the subtraction of the scattering profile generated by an empty cell. As can be seen in Figure 3.2 a pronounced peak is visible at scattering vector lengths of 3.6 nm^{-1}. This peak is from the Kapton tape used to seal the vacuum tubes before and after the sample stage at ELETTRA. It is not possible to fully remove the peak by subtraction of the empty cell. Hence, in the following scattering data presented in this work, this peak might be visible but it is not considered in the quantitative analysis (e.g. $\tilde{I}_{Bragg}$).

Looking at the curve at high q values (>6 nm^{-1}) of the profile presented in Figure 3.2, the slope of the curve changes and the intensity rises again. This is due to a peak corresponding to scattering from the amorphous polymer at higher scattering vector lengths. Thus, this apparent rise in intensity is removed. A power law in combination with a constant similar to the Porod's law described in Equation 3.1.1 is used for the fit of this section. The exponent α for the fit is estimated to be between -3 and -4 and the value of the constant is estimated with the smallest value for all q >6 nm^{-1}. The methods and functions from the Python package LMFIT [37] are used for all fits. It used non-linear least-square minimization to reduce the difference between data points and fit. In Figure 5.1 a) the data points, fitted curve and the corrected data are presented for this step. Note that only the exponential term is subtracted not the constant.

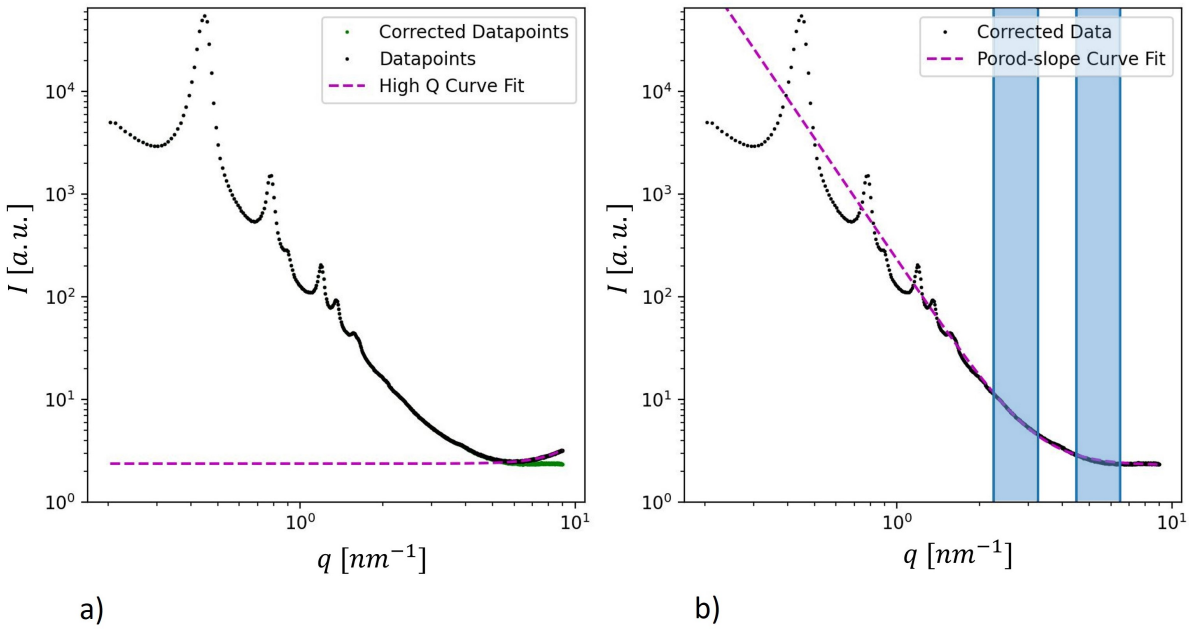

Figure 5.1: a) representative SAXS profile before and after correction at high q values, b) representative SAXS profile for the power law fit of the Porod region (i.e. highlighted area)

Next, the slope of the curve in the Porod region is determined. Similar to the previous step, Equation 3.1.1 is used with the estimation for α between [3,4]. As an estimation of the constant of this fit, the value of the constant from the previous fit is used. Values for alpha are chosen as such because the slope is not always to the power of 4 and thus it is assumed that the interface does not remain sharp for the duration of the in-situ experiment. By analyzing the exponent over the duration of the thermal treatment one can learn about changes at the interface [30, 31]. The area, as well as the result, of the evaluation is highlighted in Figure 5.1 b).

To reliably fit the data, at first only the (10) peak is fitted with a Pseudo Voigt model for each data set within one heat treatment measurement. The peak position is used to calculate the lattice constant and the expected positions of other peaks following a perfect hexagonal lattice using Equation 3.1. These values are used for the estimation of the peak position. Peaks are fitted in pairs of two ([(11),(20)],[(21),(30)],[(22),(31)]) except for the (10). This is necessary due to the difficulty to fit all peaks simultaneously when the peak intensity reduces. For more reliable fitting the intensity is multiplied with q^2. In Figure 5.2 a successful fit is displayed. The colored areas correspond to the areas used for fitting the peaks. Additionally, the calculated peak positions as well as the backgrounds are visualized.

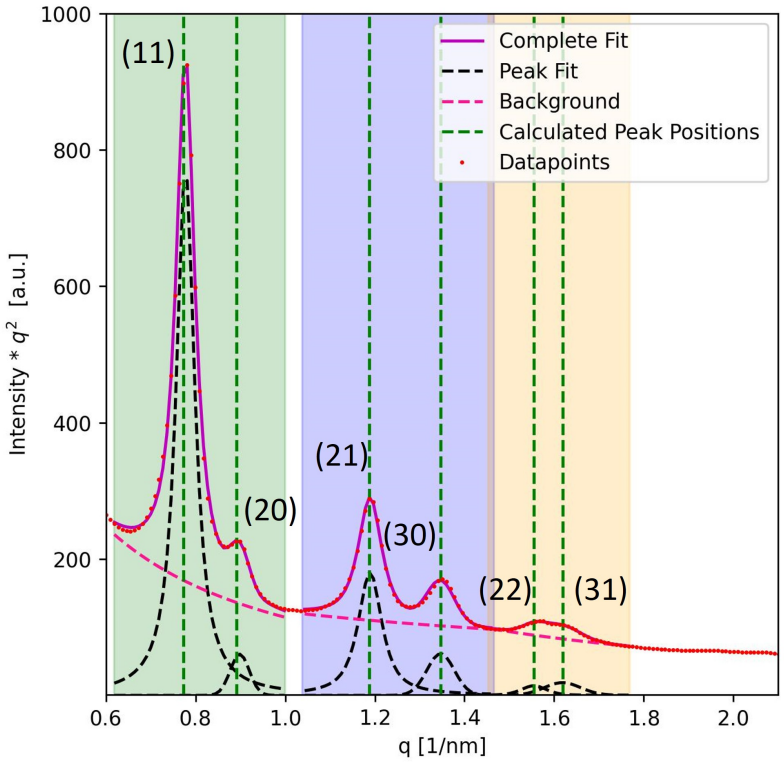

Figure 5.2: Example of pairwise peak fit with highlighted fit areas, background, and curves of fitted peaks with and without background

The fitting of all Bragg peaks is done with a Pseudo Voigt model. A linear spline in the $I(q)q^2$ vs q plot is used for the background (Figure 5.2 dashed magenta line). It is calculated with the $I(q)$ and q values at the border of the colored areas. In the case of the (21) and (30) peaks, a second linear spline is needed to model the background. The spline slopes are estimated with an additional point at a minimum intensity between these two peaks. With these three points, two slopes are calculated and summed up resulting in the dashed magenta line in the blue area highlighted in Figure 5.2.

Afterwards, the position change of the maximum of the first peak is calculated relative to the starting condition. This is used to estimate the movement of the other peaks, since in an assumed perfect lattice all peaks experience the same shift. This is used to move the areas of the peak fits according to the first peak. The sigma values as defined for the Pseudo Voigt model by LMFIT [37] are also estimated for all other data sets relative to the fitted values from the first fit. With all these conditions and estimated parameters the script can calculate every data set. These calculations are done on multiple processing cores to reduce time.

An example of these fitted peaks is displayed as a black dashed line in Figure 5.2. The area under these curves is calculated and corresponds to the integrated intensity described in Equation 3.1.1 and highlighted in Figure 3.2. This is done by using the Simpson integration with the Python library SCIPY [38].

The data is integrated with the fitted point of each peak corresponding to $I(q)q^2$ over every corresponding q value. The sum of each individual integrated peak intensity ($\tilde{I}_{hk}$) is integrated Bragg intensity ($\tilde{I}_{Bragg}$).

The same approach is applied to all curves displayed in Figure 5.1 b), resulting in the total integrated scattering intensity ($\tilde{I}$). When $\tilde{I}_{Bragg}$ is subtracted from $\tilde{I}$ the integrated diffuse intensity ($\tilde{I}_{diff}$) is calculated. A visual representation of $\tilde{I}_{Bragg}$ is given in Figure 3.2 as the blue highlighted part of the curve. The rest of the profile is $\tilde{I}_{diff}$.

5.2 Form Factor Fit

Using the formulas described in chapter 3.1.2 two models are used to fit the in-situ SAXS profiles. For this, Equation 3.1.2 is minimized with the non-linear least-square method of LMFIT [37]. The automated fitting of the form factor turned out to be challenging. The one-step model is easier to fit due to the reduced amount of fitting parameters. For the two-step model, it is possible to achieve similar χ^2 values for multiple combinations of parameters. As the radius gets larger the Bessel function oscillates faster, yielding an incorrect result but with the same or even better accuracy. To compensate for this, parameters had to be restricted in their freedom. Another trick used, is to express the second radius as $R_1 = R_0 + t$ with t as the thickness of the shell. This is easier and faster to incorporate into the program, than including the condition $R_0 < R_1$ explicitly.

One problem is also that if a parameter is changed slightly during the fit and the new fit is calculated and compared to the previous one, there is no clear convergence for the change in parameters. All of these issues lead to the realization that it is not possible to fit a whole measurement in a recursive manner. For the two-step model, an approach is chosen that drastically increased the calculation time but makes it possible to fit all data sets of a measurement. Each parameter is changed by $\pm$ 1,3,5,7,9 % and a fit is performed where all parameters can be changed by $\pm$ 5 %. This ensured that the generated values by a misfitted data set can be corrected in the next fit. After calculating the fits of each interpolation of these changes the fit with the smallest χ^2 is chosen as the best fit and as the starting values for the manipulations of the next. This improved the fitting for the two-step model but as it can be seen in Figure 5.3 the best fit for the two-step model still is sometimes a faster oscillating curve.

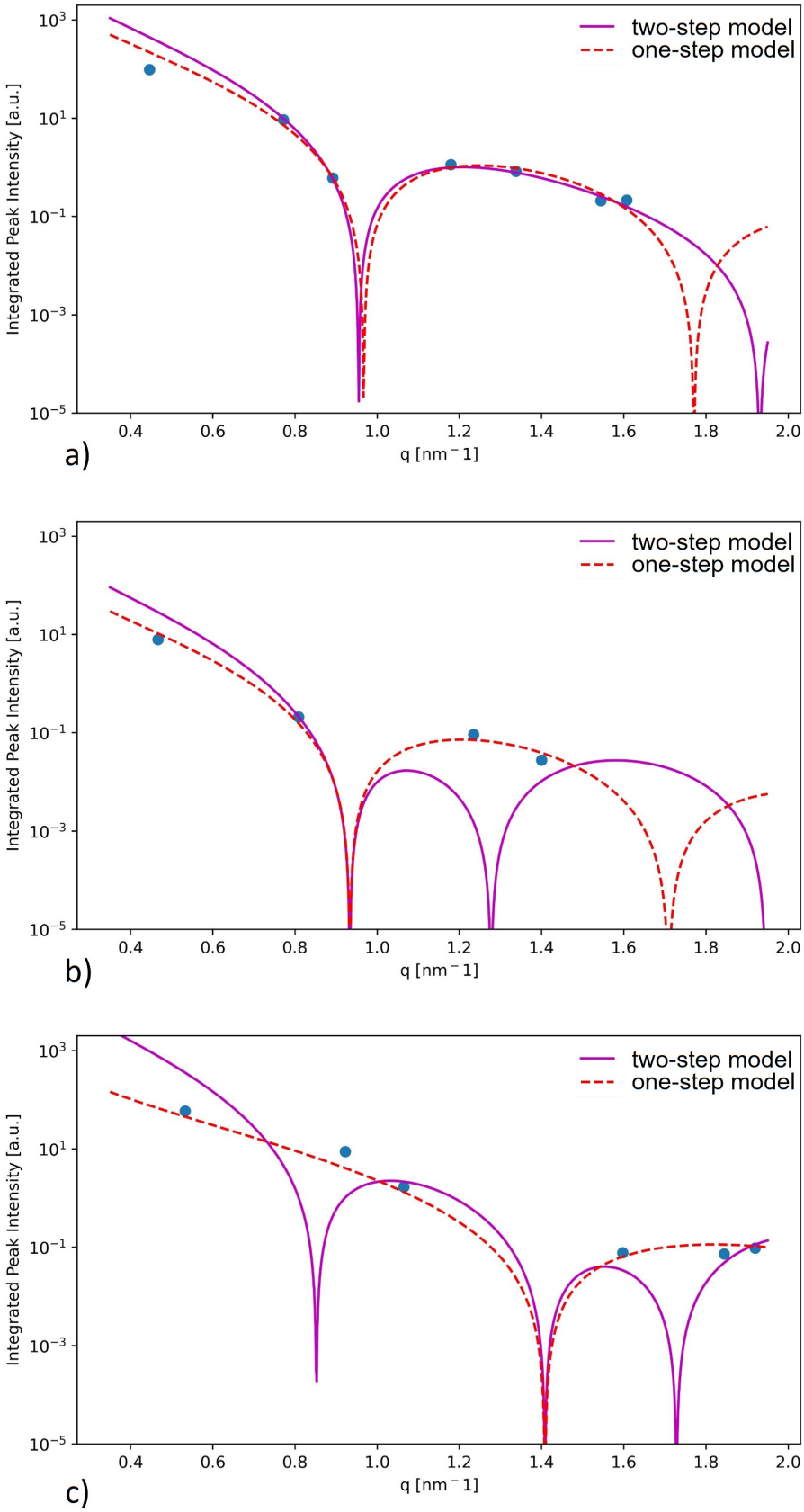

Figure 5.3: Single- and two-step model fit, a) example of good fits, b)-c) good fit for single-step model and bad fit for two-step model

6 Results and Discussion

In this chapter, all results of this work are presented. The main goal of this thesis is to optimize the mesostructure. However, it is also useful to understand and investigate the structural properties up to the macroscopic level. The macroscopic information complements the structural investigations and can be used to understand its behavior in future applications.

6.1 Macroscopic Structural Information

In Figure 4.3 the uncalcinated STC monolith is visible after some samples are already prepared. Looking at the edge, remaining after cutting it in two, one can see that the color of the material is not homogeneous throughout the sample. For investigations of the macro- and mesostructure using complementary imaging techniques, SEM images (produced and provided by the "Lehrstuhl für Metallkunde und metallische Werkstoffe" at Montanuniversität Leoben) and TEM images (produced and provided by the "Lehrstuhl für Nichteisenmetallurgie" at Montanuniversität Leoben) of the STCs in carbonized condition are presented in Figures 6.1 a)-d). As can be seen in the SEM images, the material consists of rod-like carbon struts that are connected in joints.

In the TEM images a single strut is imaged at a higher magnification. An ordered array of brighter and darker lines is clearly visible. Depending on the imaging mode the brighter lines correspond to the mesopores in the carbon matrix or to the matrix itself. Figure 6.1d) is taken as a high-angle annular dark field image. In such images the matrix (with higher atomic number) is bright while the mesopores (with lower atomic number) are dark. The TEM images clearly show that the pore length is far longer than the pore diameter. Therefore, infinitely long cylinders are assumed for the form factor fit. Due to the insufficient resolution and unknown orientation of the rods within the observed strut, exact dimensions can not be extracted from the TEM images. However, it is possible to compare the widths between the darker and brighter lines. Depending on the sample tilt, pore distances might appear distorted, but as a rough estimate one can assume the distance between to pores to approximately equal two times the pore diameter.

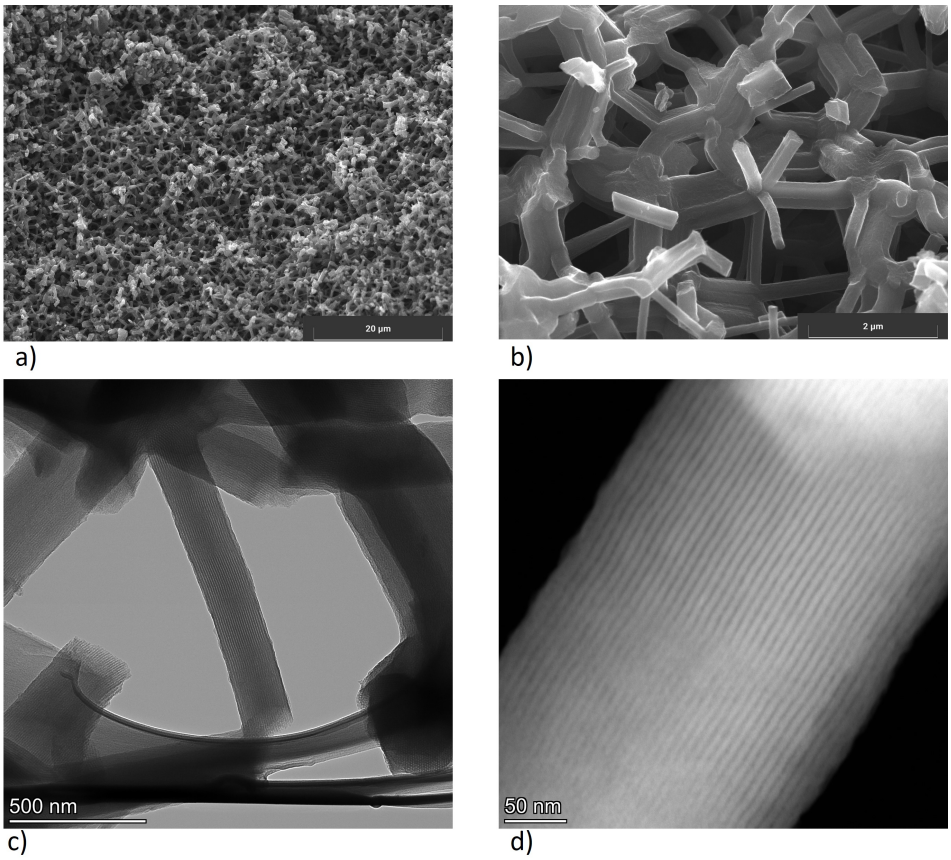

Figure 6.1: Images of STC calcinated at 280 $°C$ for 30 min (O_2 2-5 %, 3 $°C/min$) and carbonized at 850 $°C$ for 1 h (Ar,1 $°C/min$), a)-b) SEM images in secondary electron contrast, c)bright field TEM image, b) high-angle annular dark field TEM image

Within a joint, the visible lines become entangled and distorted. It is possible that the two-dimensional hexagonal structure within these joints cannot be maintained with the same quality as in the struts. These images also depict the macro porosity in the uncalcinated STC. The empty space is a result of the strut- and joint-like arrangement creating a lot of macropores. The skeletal density ρ_s is estimated with Helium Pychnometry (produced and provided by the "Institut für Chemie und Physik der Materialien" at the Paris Lodron University Salzburg) to be about 1.15 g/cm^3 and with a bulk density ρ_b of 0.3 g/cm^3.
The porosity is calculated with [35]:

$$Porosity = \frac{\rho_s - \rho_b}{\rho_s} \tag{6.1}$$

Resulting in a porosity of 74 % for the uncalcinated condition.

6.2 Structural Investigation of the uncalcinated STC

The majority of the structural investigation in this thesis is performed with in-situ SAXS measurements. A complete list of the in-situ experiments and their heat treatment conditions is presented in Table 6.1. The experiment label is composed of the holding temperature (HT+holding temperature in $°C$) plus the oxygen content (O+oxygen content in oxygen nitrogen mixture in %) plus the heating rate (R+heating rate in $°C/min$). If an in-situ sample is heated under pure N_2 atmosphere the label "N2" is added before the oxygen content and the oxygen content refers to the content after reaching HT. The samples highlighted in purple in Table 6.1 are used for quantitative analysis. The samples highlighted in cyan are of limited reliability due to issues during the measurements (see the comments in Table 6.1)

The samples investigated in the in-situ experiments are taken from different positions of the monolith. It is unfortunately not possible to correlate each sample to its exact position but, after sample 14 all samples are taken from the center region highlighted in green in Figure 6.2. This is important, since it appeared that the density and thus, possibly also the microstructure is different at the edge of the monolith.

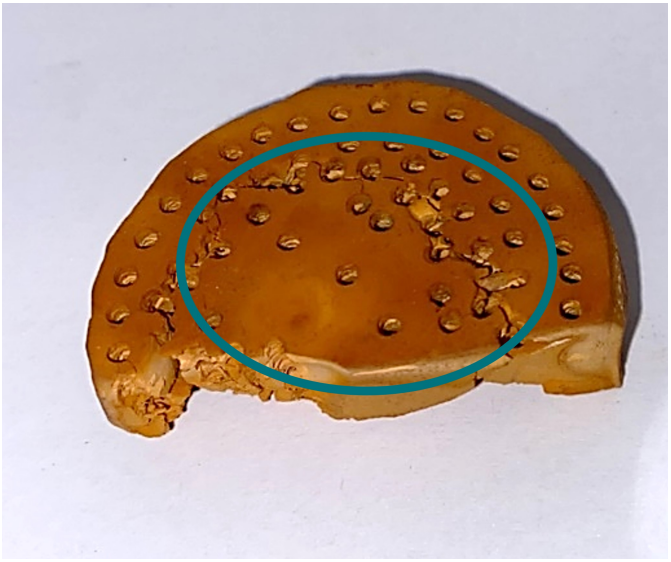

Figure 6.2: Uncalcinated STC monolith, in-situ samples 13-22 are taken from the highlighted area

Sample Index	Experiment Label	Average Holding Temperature [$°C$]	Heating Rate [$°C/min$]	O_2 [%]	Gas Flow [L/min]	Heating under N_2	Data Evaluation Successful	Comment
1	HT 328 O10 R3	328	3	10	1	No	No	Sample is blown out of beam at the end of the measurement
2	HT 334 O10 R3	334	3	10	1	No	Yes	Problems with beam intensity drop during the measurement
3	HT 302 O2 R3	302	3	2	0.5	No	No	Low intensity in ionisation chamber, pinhole is moved and not corrected
4	HT 307 O2 R1	307	1	2	0.5	No	No	Same problem as with previous
5	HT 300 O10 R3	300	3	10	0.5	No	No	/
6	HT 300 O2 R3	300	3	2	0.5	No	Yes	/
7	HT 304 O10 R3	304	3	10	0.5	No	Yes	/
8	HT 280 O10 R3	280	3	10	0.5	No	Yes	/
9	HT 340 O10 R3	340	3	10	0.5	No	Yes	/
10	HT 245 O2 R1	245	1	2	0.5	No	Yes	Measurement is stopped early
11	HT 243 O10 R3	243	3	10	0.5	No	Yes	Many room temperature measurements because oven is not turned on
12	HT 273 O2 R3	273	3	2	0.5	No	Yes	Pinhole is adjusted
13	HT 259 O2 R3	259	3	2	0.5	No	Yes	After 206.3 *min* 10% O_2 and after 236.6 *min* 21% O_2, values after 206.3 *min* are excluded for the evaluation
14	HT varied O2	multiple	costume	2	0.5	Yes	No	Sample is heated under N_2 in multiple steps, after 231.6 *min* 2% O_2, after 359 *min* 10% O_2, after 399 *min* 2% O_2, after 479.6 *min* 10% O_2, after 485.3 *min* 21% O_2
15	HT 275 O2 R1	275	1	2	0.5	No	Yes	/
16	HT 275 N2 O10 R3	275	3	10	0.5	Yes	Yes	10% O_2 after 100 *min*
17	HT 275 N2 O2 R3	275	3	2	0.5	Yes	Yes	two different oxygen mixtures used, 10% O_2 after 112 *min* and corrected to 2% O_2 after additional 10 *min*
18	HT 294 N2 O2 R10	294	10	2	0.5	Yes	2% Yes	O_2 after 40.7 *min*
19	HT 260 N2 O2 R10	260	10	2	0.5	Yes	Yes	2% O_2 after 43 *min*
20	HT 275 N2 O2 R3	275	3	2	0.5	Yes	Yes	2% O_2 after 85.7 *min*
21	HT 340 N2 O2 R10	340	10	2	0.5	Yes	Yes	2% O_2 after 42 *min*
22	HT 274 N2 O10 R10	274	10	10	0.5	Yes	Yes	10% O_2 after 35.3 *min*

Table 6.1: Table of all in-situ experiments performed at ELETTRA, highlighted in purple are all experiments used for quantitative analysis, highlighted in cyan are all experiments where the data analysis is successful but some problems (see comments) arose which mean that the assumptions made when looking at these samples have limited reliability

In order to estimate the structural differences within the in-situ investigated samples and their effects on the SAXS derived values, the calculated parameters of each measurement are averaged over the first ten data points and presented in Table 6.2. These values correspond to room temperature measurements of each in-situ data set. Table 6.3 shows the mean and the standard derivation of the total samples measured.

The standard derivation of the integrated Bragg intensity and the total integrated intensity is relatively high, while the other presented values are significantly smaller. The standard derivation of $\tilde{I}_{Bragg}$ is 27.80 %. This indicates a heterogeneity on a nanoscopic scale. To understand this heterogeneity the plot displayed in Figure 6.3 is created. Comparing the integrated Bragg intensity with the power law exponent α described in Equation 3.1.1 of each sample, a correlation between these two values is indicated. This implies that the difference between each sample is caused by the heterogeneity of the triblock polymer and its interface with the RF matrix.

Since the exponent α varies for the samples taken from monolith either the surfactants are sometimes structurally distorted or the interface is somehow different. The apparent correlation of these two values indicates that the variations are mainly caused by differences in the interface. They may be due to an increase and decrease in electron density difference between interface and matrix. A more thorough discussion of these deviations will follow in the next chapter.

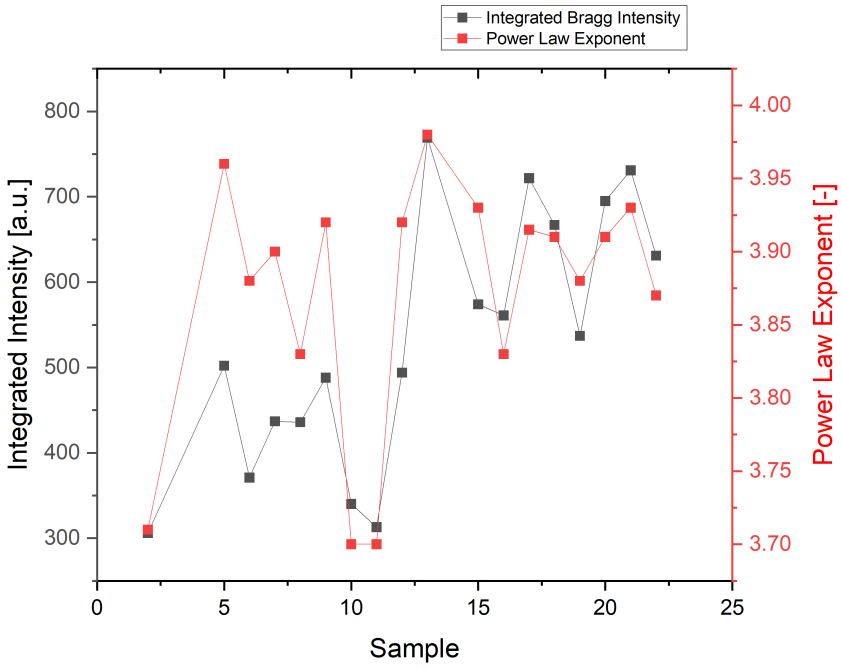

Figure 6.3: Comparison of integrated Bragg intensity and power law exponent at room temperature

Experiment Label	Integrated Bragg Intensity [a.u.]	Integrated Diffuse Intensity [a.u.]	Total Integrated Intensity [a.u.]	Full width half maximum of (10) peak $[1/nm]$	Power Law Exponent [-]
HT 334 O10 R3	306	743	1049	0.05022	3.71
HT 300 O10 R3	502	813	1316	0.03947	3.96
HT 300 O2 R3	371	743	1115	0.05299	3.88
HT 304 O10 R3	437	795	1231	0.04955	3.90
HT 280 O10 R3	436	799	1236	0.05005	3.83
HT 340 O10 R3	488	755	1243	0.04251	3.92
HT 245 O2 R1	340	778	1118	0.04987	3.70
HT 243 O10 R3	313	766	1080	0.04917	3.70
HT 273 O2 R3	494	853	1347	0.04892	3.92
HT 259 O2 R3	769	868	1637	0.04638	3.98
HT 275 O2 R1	574	866	1440	0.04449	3.93
HT 275 N2 O10 R3	561	866	1427	0.04903	3.83
HT 275 N2 O2 R3	722	907	1630	0.0458	3.88
HT 294 N2 O2 R10	667	773	1440	0.04425	3.91
HT 260 N2 O2 R10	537	727	1264	0.04358	3.88
HT 275 N2 O2 R3	695	835	1530	0.04329	3.91
HT 340 N2 O2 R10	731	824	1556	0.04354	3.93
HT 274 N2 O10 R10	631	841	1471	0.04562	3.87

Table 6.2: Room temperature measurements averaged over the first 10 data points

Integrated Bragg Intensity of Peaks [a.u.]	Integrated Diffuse Intensity [a.u.]	Total Integrated Intensity [a.u.]	Full width half maximum of (10) peak $[1/nm]$	Power Law Exponent [-]
520.7±144.7	802.6±47.4	1323.5±177.1	0.0466±0.0036	3.87± 0.09

Table 6.3: Average room temperature measurements with standard derivation

Since samples 14-22 show a similar behavior, it is reasonable to assume a correlation with the sample positions described in Figure 6.2 above, meaning that the samples are taken from the center region of the monolith. The starting difference can been reduced if all samples are taken from the center region.

The difference in $\tilde{I}_{Bragg}$ can be caused by the variation of the amount of hexagonal arranged irradiated pores. The relatively low standard derivation of $\tilde{I}_{diff}$ indicates that the general scattering of the material is rather homogeneous. It indicates that the differences in the hexagonal pore structure do not have major influence on the diffuse scattering. This provides reasonable information to assume that it is possible to divide the integrated intensity into $\tilde{I}_{Bragg}$ and $\tilde{I}_{diff}$ to individually describe the changes in the matrix.

In Table 6.4 the lattice constants calculated from each peak of a representable measurement are shown. The values are once again averaged over the first 10 data points at room temperature. If the lattice constants differ, it can indicate a distorted hexagonal lattice with a higher lattice spacing in one direction than the other.

a_{1_0} $[1/nm]$	a_{1_1} $[1/nm]$	a_{2_0} $[1/nm]$	a_{2_1} $[1/nm]$	a_{3_0} $[1/nm]$	a_{2_2} $[1/nm]$	a_{3_1} $[1/nm]$
16.28	16.17	16.15	16.16	16.16	16.16	16.16

Table 6.4: Lattice constants calculated from each peak position and averaged over the first 10 data points for sample *HT 275 N2 O2 R3*

The first peak differs from the other peaks by about 0.68 %. This is most likely not a lattice distortion but rather a result of the fitting. As can be seen in Figure 5.1, comparatively few data points are generated in the q range of the (10) peak. This can explain why the fit had a lot of difficulties with the first peak, resulting in a slight increase in the apparent lattice constant. All these result confirm the hexagonal arrangement of the surfactans with a cylindrical shape.

6.3 Structural Changes during Calcination

During calcination the soft template is removed from the carbon precursor. After an ideal calcination treatment only the template is removed, leaving the empty two-dimensional hexagonal arranged mesopores behind. In order to describe and evaluate the changes during calcination, various values are derived using the costume Python script described in chapter 5.

The lattice constant (orange colored dots in Figure 6.4) calculated from the (11) peak is used for the following quantitative analysis. As described in the previous chapter the difference between the lattice constants is insignificant indicating a non distorted two-dimensional hexagonal lattice. The lattice constant described the distance between two pore centers. The change of this parameter thus correlates to a shrinkage or swelling of the overall mesostructure. It is expected that the matrix shrinks and subsequently the lattice constant reduces after complete calcination due to further compactation of the RF matrix and building of polymer networks.

Another investigated characteristic length is the (filled) mesopore radius (red colored dots in Figure 6.4) derived from the single-step from factor model. This value indicates the apparent size of the (filled) mesopore in the matrix. It does not distinguishes between filled or empty mesopores. This value should exhibit a fast change during the template removal. After complete calcination it is expected to decrease similar to the lattice constant.

The power law exponent α (blue dots in Figure 6.4) derived form the the slope at high q values (Porod region as described in chapter 3.1) can be used to describe the changes of the interface between the matrix and the (filled) mesopore. A sharp interfaces would have an exponent of 4. Smaller values can indicate the existence of surface roughness or micropores at the mesopore walls.

The electron density difference $\Delta\rho$ (gray colored dots in Figure 6.4) derived from the single-step form factor model is proportional to the SAXS contrast between the matrix and the (filled) pore. This value is expected to increase after calcination due to the higher contrast between matrix and air compared to matrix and surfactant.

Hence, it can indicate template removal. In addition it can indicate possible changes within the filled mesopore space during heating. The integrate Bragg intensity (magenta colored dots in Figure 6.4) is a value that depends on multiple factors. It is influenced by the contrast between the matrix and the (filled) pore, described by $\Delta\rho$. If the electron density difference decreases so does $\tilde{I}_{Bragg}$. Additionally, any deviation from the ordered arrangement of rod-like (filled) pores in a two-dimensional hexagonal lattice reduces this value. Possible structural changes that result in a deviation from the ideal arrangement include the removal of walls between the mesopores.

The last value used for the quantitative analysis is the integrated diffuse intensity (green colored dots in Figure 6.4). There are many contributions to this value, including the electron density of the matrix and the existence of randomly arranged micropores.

The evolution of all above described values during a calcination treatment are shown in Figure 6.4. This multiaxial plot is created for an in-situ sample heated with a heating rate of 3 $°C/min$ to a temperature of approximately 275 $°C$ under nitrogen gas flow. After 86 min, when the holding temperature is reached the synthetic air is added to the nitrogen gas flow, resulting in a mixture of 2 % O_2 and 98 % N_2.

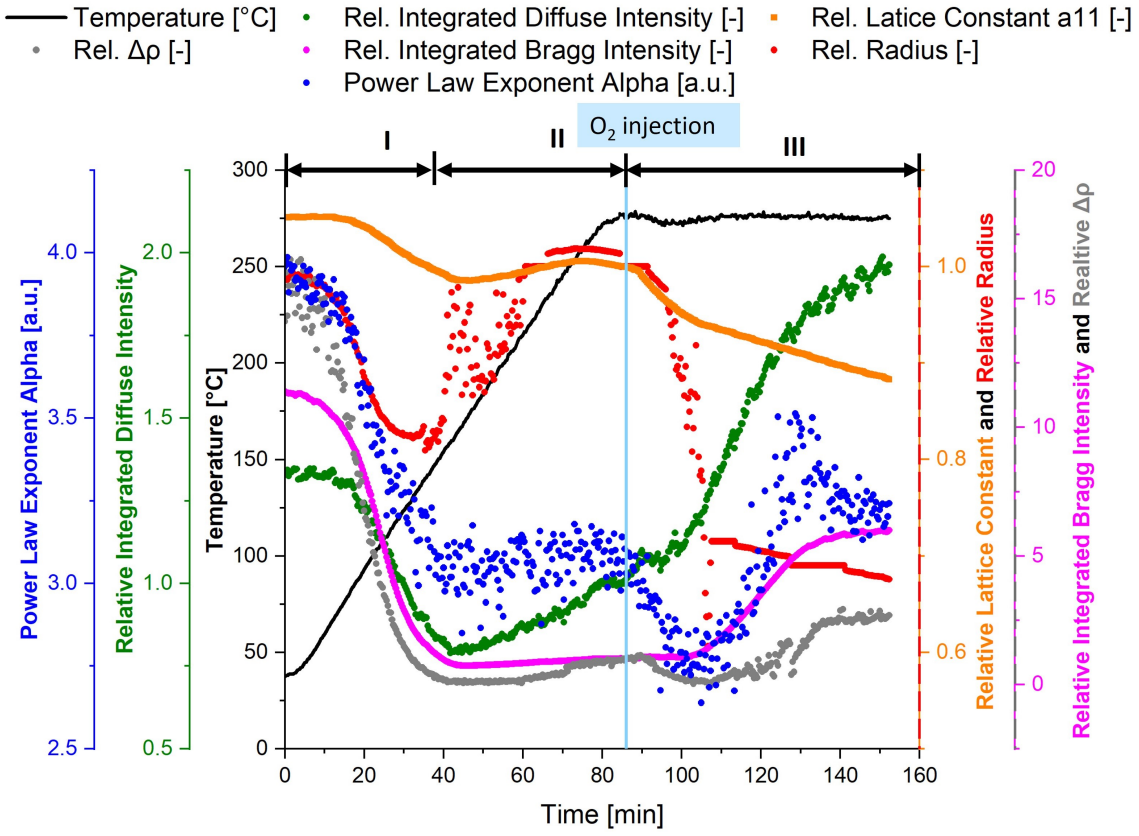

Figure 6.4: Comparison of derived parameters for in-situ sample *HT 275 N2 O2 R3*, the start of the oxygen injection (vertical blue line), removal of water at the interface (region I), swelling of the carbon precursor (region II), removal of surfactant (region III)

As previously described the samples are not homogeneous and thus also the SAXS derived parameters are not strictly comparable on an absolute scale. Therefore, all values, except for the power law exponent, are relative to the values right before oxygen is injected. In this multiaxial plot in Figure 6.4, which is representative for all samples heated only under nitrogen atmosphere, three distinct regions can be identified.

Region I is identified as the region of water removal at the interface of the filled pore and the matrix. The power law exponent is about 4 at room temperature while the integrated Bragg intensity and the electron density difference experience an overall maximum value. All values are relatively unchanged during the initial heating stage. At around 90 $°C$ nearly all values start decreasing, except the lattice constant which starts reducing at about 110 $°C$. The changes of all these values and the temperature range where this effect occurs indicate that water is removed from the interface between the surfactant and the matrix. Water at the interface can both explain the apparent sharp interfaces as well as the $\Delta\rho$ and $\tilde{I}_{Bragg}$ values at room temperature. It is likely that the water is incorporated between the triblock polymer and the carbon precursor during synthesis. Viewing the schematic representation of F127 in the uncalcinated condition, depicted in Figure 2.3 the water would be at the hydrophilic ends, between the individual polymer strands and possibly in the matrix.

Figure 6.5 is a TGA curve with the same targeted holding temperature and heating rate as the in-situ sample in Figure 6.4. Right before oxygen injection, a mass loss of 4.5 % can be identified. The removal of water during calcination of SBA-15 [39], a structurally similar but silica based material, has been reported. This aids the assumption that water is removed during the heating of the material.

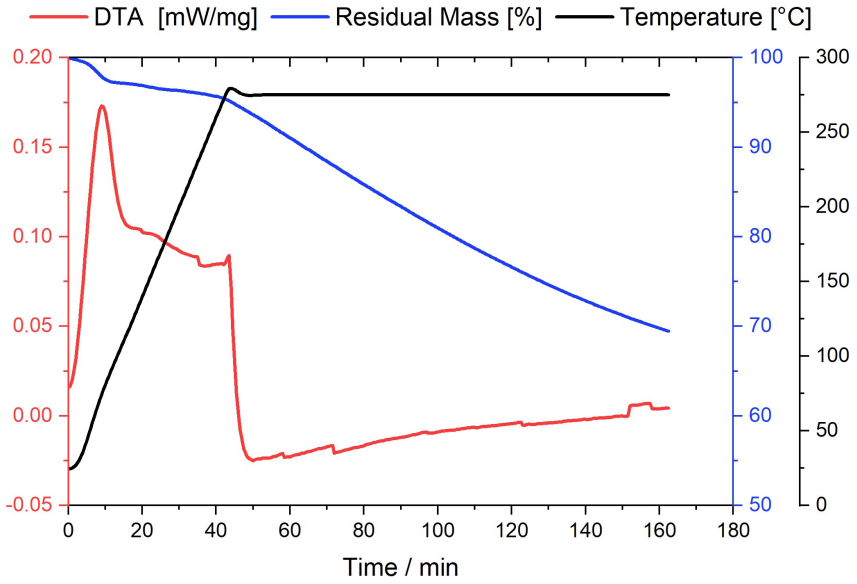

Figure 6.5: TGA of calcination with similar conditions as in-situ sample *HT 275 N2 O2 R3*

Region II defines a region where the carbon precursor material experiences swelling. This is indicated by the increase in the relative pore radius as well as the relative lattice increase significantly. Multiple swelling effects of polymers have been reported [40], especially during gas adsorption measurements with nitrogen [41]. Another effect that can contribute to this is thermal expansion. The exact reasons for swelling, in this case, cannot be concluded within the scope of this thesis.

However, it is found that while there is a change in the material (as indicated by the change of $\Delta\rho$ and $\tilde{I}_{diff}$) there is no change at the interface (as indicated by α) nor on the two-dimensional hexagonal structure (as indicated by the $\tilde{I}_{Bragg}$).

The third region is identified as the removal of the surfactant. At the start of this region the pore radius, the lattice constants as well as the power law exponent is reduced quickly. This indicates that at the start of the template removal the material shrinks down rapidly while the integrated intensities do not change in their behavior. They only change after a minimum is reached for the power law exponent. After this characteristic point there is a fast increase of the integrated Bragg intensity and the electron density difference. This indicates the successful removal of the template. The change of the slopes of the lattice constant as well as the pore radius after this point further indicates successful removal. As is expected the slopes at the end of region III for both values are similar indicating a homogeneous shrinkage. The increase in $\tilde{I}_{Bragg}$ can be explained by the compactation of the carbon precursor and the building of polymer networks. This is indicated by the increase in electron density difference.

Due to the correlation found between the change in the slope of the lattice constant and the indicated complete removal of the surfactants in Figure 6.4, a new graph (Figure 6.6) is created comparing the slopes of the lattice constants for the samples heated under nitrogen. It indicates that the slope of the lattice constant changes at similar values except for the one experiencing the highest temperature. The existence of this changing point for multiple temperatures indicates that the surfactant removal can be controlled up to a temperature of roughly 300 $°C$. At higher temperatures, the reaction is too fast to reliably set the desired structural parameters.

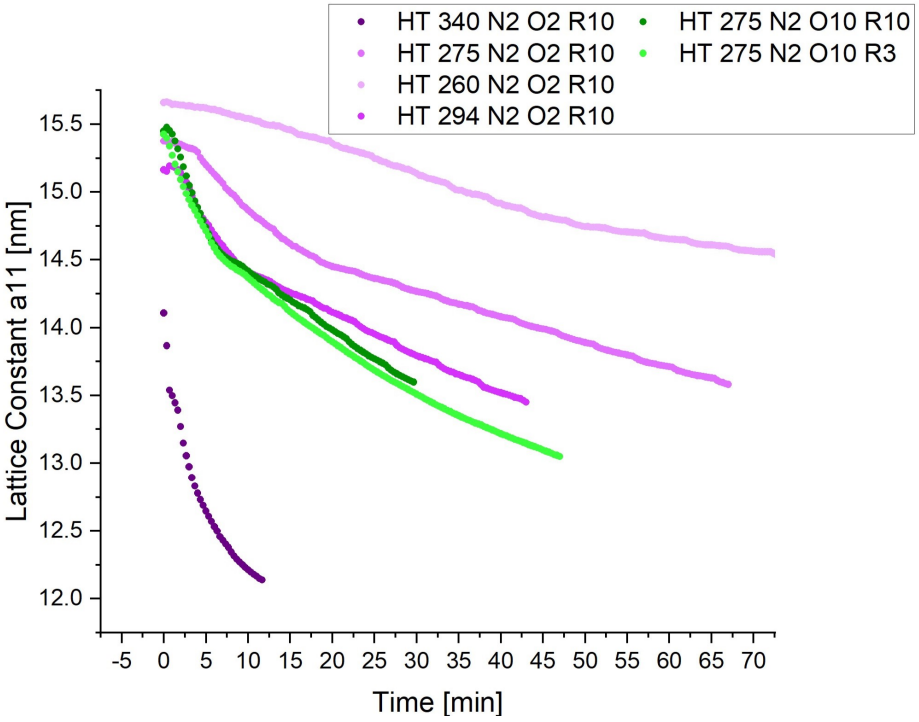

Figure 6.6: Comparison of lattice constant evolution for in-situ samples heated under N_2 gas flow

In Figure 6.7 in-situ sample *HT 340 O10 R3* is also represented in a multiaxial plot. This samples can heated under gas flow containing 10 % O_2 and 90 % N_2. For in-situ samples heated under oxygen containing gas flow the SAXS derived parameters are relative to the values at 240 $°C$. This is done because under these conditions at 240 $°C$ the shrinkage and and reduction in peak intensity have reached a more or less stable value, making it possible to compare the samples heated under oxygen with each other. Figure 6.7 represents what happens after successful template removal has occurred. After a local maximum in relative integrated Bragg intensity (successful template removal) is reached, $\tilde{I}_{Bragg}$, the power law exponent as well as $\tilde{I}_{diff}$ decrease. This information lead to the assumption that after complete surfactant removal the structural integrity is reduced. The hexagonal arrangement seems to be destroyed slowly (indicated by $\tilde{I}_{Bragg}$ and power law exponent) and possibly precursor material is removed (indicated by $\tilde{I}_{diff}$).

Findings made by Florek et al. [42] while investigating the change of the microstructure of SBA-15, a structurally similar but silica based material, due to hydrothermal ageing, lead to a perception of the structural deterioration of the hexagonal arrangement in this silica. Since the structure of these materials is similar to the one presented here, the change of SBA-15 can be used and applied on the STC. Using the findings in this work, leads to a similar perception of the structural changes after complete removal has occurred and the temperature and oxygen flow is still provided. The assumed change of the mesostructure is depicted in Figure 6.8 and is similar to the descriptions made in Florek et al. [42].

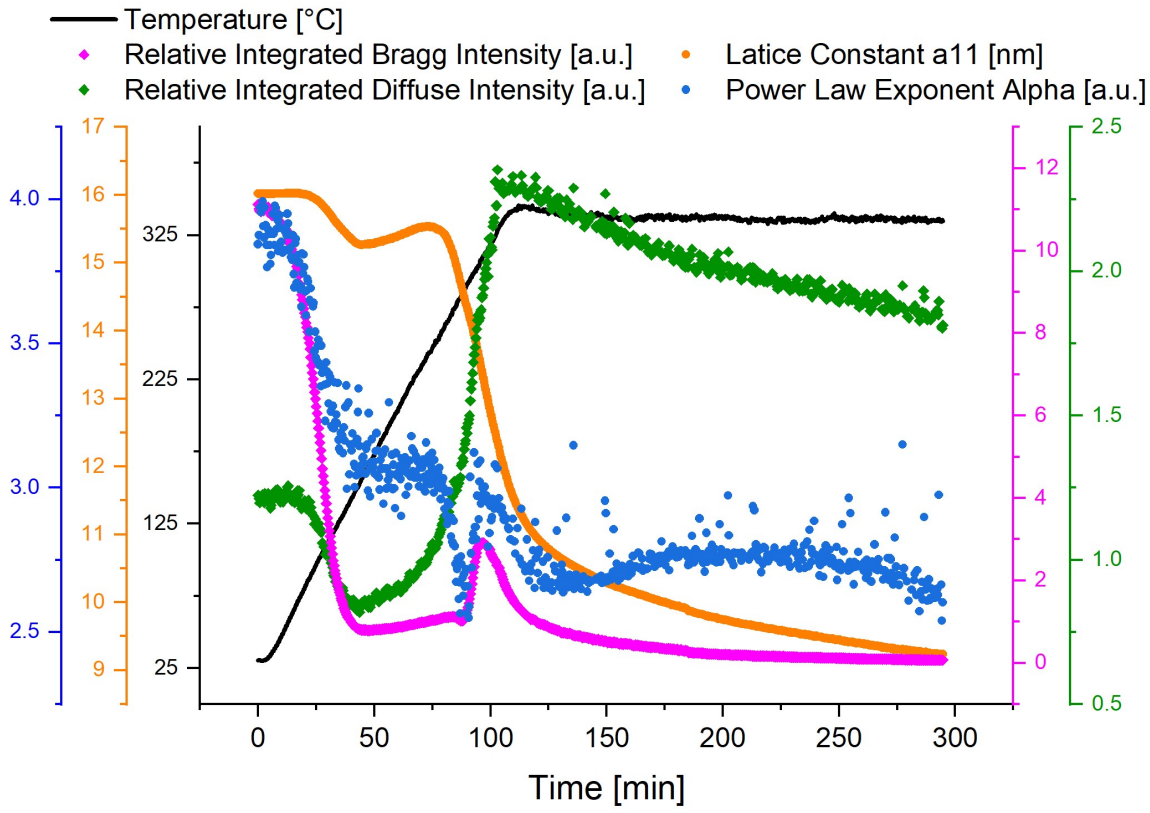

Figure 6.7: Multi axial graph of *HT 340 O10 R3*

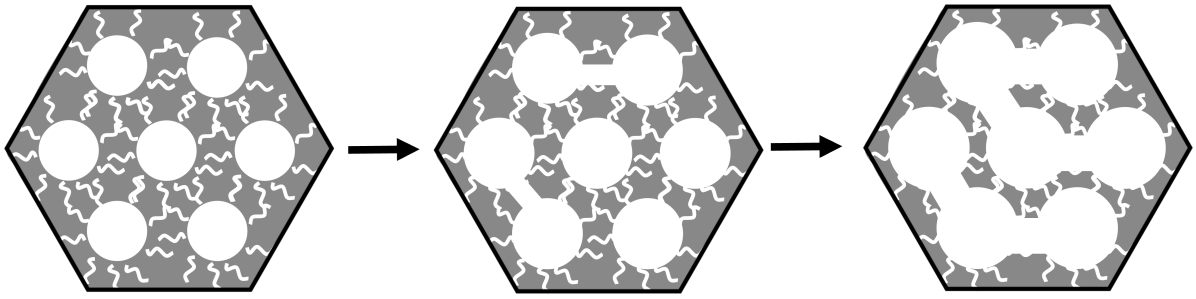

Figure 6.8: Possible structural changes during heat treatment after template removal similar to [42]

6.4 Gas Adsorption Analysis

For the gas adsorption measurements more calcinated material is required than is available from the in-situ measurements. The samples are therefore called ex-situ samples and are calcinated not by the in-situ SAXS set-up but in a TGA device. Theses samples and their respective final masses measured with the TGA, as well as some derived gas adsorption values are described in Table 6.5. The specific pore volume (V_p) is calculated by using the Gurvich rule [35] for type IV isotherms [15]. Together with the BET the average pore size can be calculated as follows [35]:

$$d_{average} = \frac{4 * V_p}{S_{BET}} \tag{6.2}$$

where:

$d_{average}$	...	*average pore diameter*
V_p	...	*total specific pore volume determined at* $\frac{P}{P_0} \approx 0.95$
S_{BET}	...	*BET surface area*

The ex-situ label sample label is composed of the holding temperature (HT+holding temperature in $°C$) plus the holding time. All ex-situ samples are heated with a heating rate of 3 $°C/min$ under nitrogen atmosphere. After HT is reached the atmosphere is set to a mixture 2 % oxygen and 98 % nitrogen. For *HT 300 °C 50 min* and *HT 260 °C 140 min* multiple samples generated in multiple heat treatments in the TGA are combined. In table 6.5 the average relative final mass and its variance are depicted. For the third measurement only one sample is prepared, so the value corresponds to this measurement.

Gas adsorption analysis is necessary to verify that the samples are indeed mesoporous after thermal treatment. In Figure 6.9 adsorption and desorption branches for these three samples, as described in Table 6.5, are depicted. The corresponding pore size distribution generated with BJH method is shown in Figure 6.10. Sample *HT 300 °C 120 min* has the highest specific BET surface area and specific total pore volume while *HT 260 °C 140 min* has the lowest. This can be correlated to the amount of mass lost during calcination. It indicates that the sample calcinated for 120 min at 300 $°C$ has more surfactants removed than the other samples, with *HT 260 °C 140 min* having the least amount of surfactant removed. *HT 260 °C 140 min* and *HT 300 °C 50 min* are ex-situ measured with SAXS and the corresponding curves are shown in Figure 9.4.

Ex-situ Sample Label	**Relative Final Mass** $[\frac{m}{m_0}]$	S_{BET} $[\frac{m^2}{g}]$	V_p $[\frac{cm^3}{g}]$	$d_{average}$ $[nm]$	d_{BJH} $[nm]$
HT 300 $°C$ 120 min	60.7	231.581	0.2398	4.14	4.856
HT 300 $°C$ 50 min	70.0 $\pm$ 1.2	63.461	0.07192	4.53	4.802
HT 260 $°C$ 140 min	77.4 $\pm$ 1.1	9.852	0.01326	5.38	4.239

Table 6.5: Relative final mass after TGA, BET area, total specific pore volume determined at $P/P_0 \approx 0.95$, average pore diameter calculated with Equation 6.2, pore diameter derived with BJH method

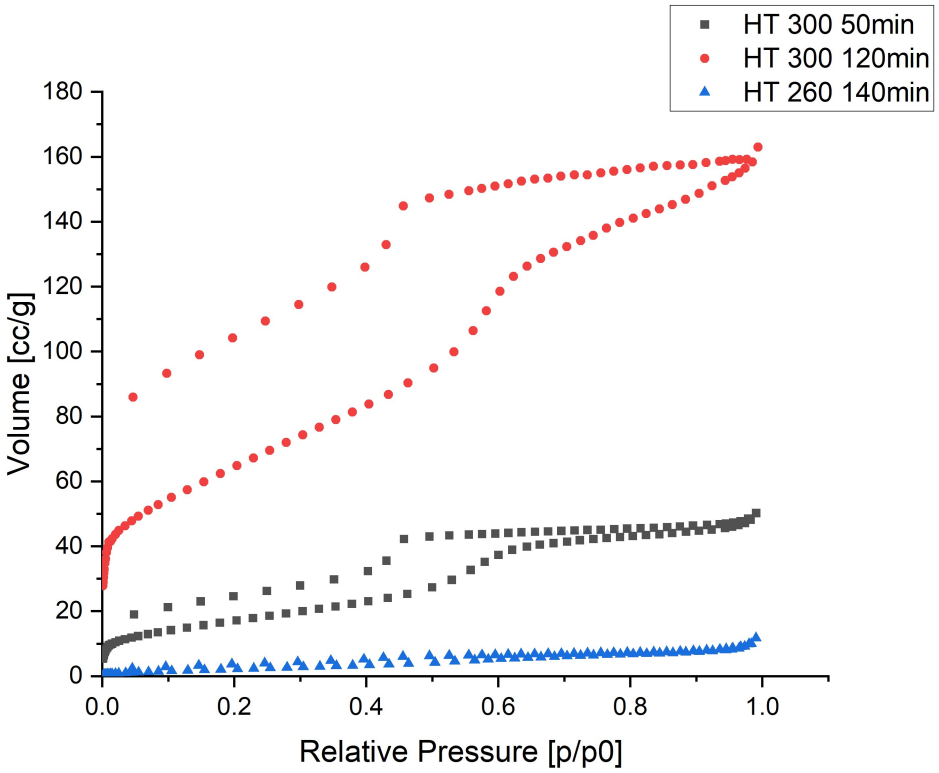

Figure 6.9: Gas adsorption isotherms for ex-situ samples in calcinated condition

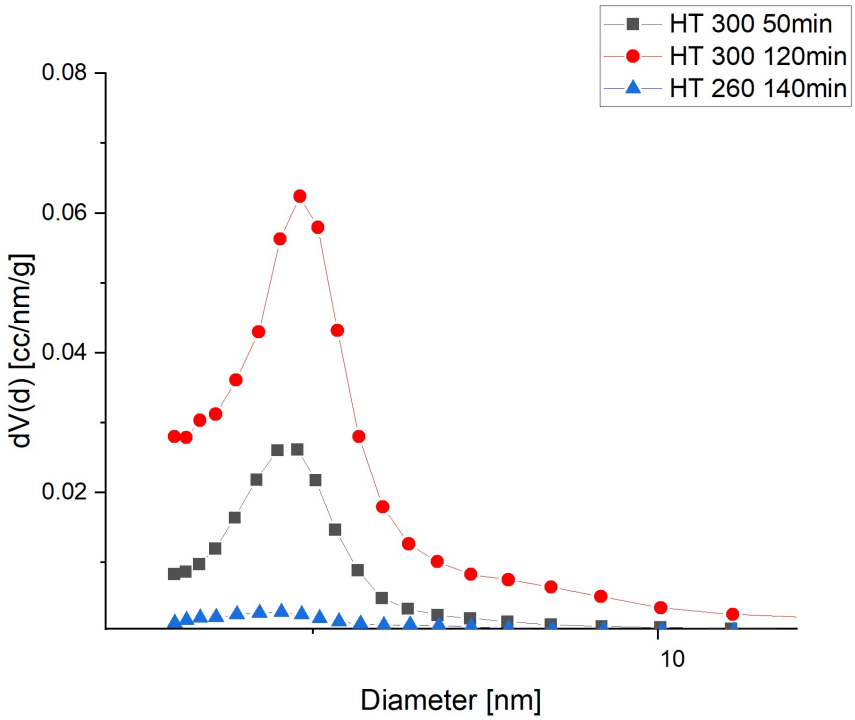

Figure 6.10: BJH derived pore size distribution for ex-situ samples in calcinated condition

It is surprising that for the same heat treatment conditions used at ELETTRA, where complete calcination is reached, such low surface area is obtained. It seems like the calcination treatment in the TGA instrument is much slower than the in-situ experiments. The difference is most likely due to the different gas flow conditions.

At ELETTRA it is possible to direct the gas through the capillary and thus directly through the sample. For the TGA the sample is put inside of a pot, as seen in Figure 4.5. In this furnace, the gas is not forced through the sample. This can lead to a slower reaction and a "top-down" calcination in the material rather than a homogeneous calcination throughout the material. This can lead to deterioration of pore walls for material at the top of the pot, while the bottom part may not be fully calcinated. This indicates that the impact of the gas flow cannot be neglected, also making the comparison of the sample calcined in the TGA with the in-situ measurements difficult. A schematic representation of the different gas flow conditions is depicted in Figure 6.11. Thus, these gas adsorption measurements did not experience the same heat treatment and are not comparable. It is only possible to extract indications for possible correlations.

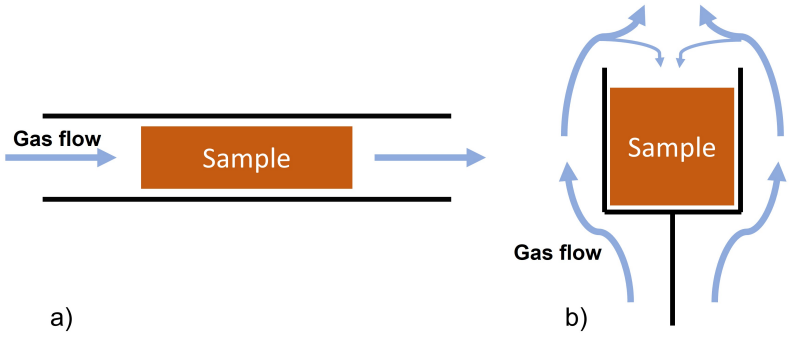

Figure 6.11: Schematic representation of the different gas flow conditions in the a) in-situ furnace, b) TGA

Taking these findings into account, the gas adsorption measurements indicate different states of F127 removal. The BET area of STCs calcinated at 300 $°C$ for 30 min under 2 % oxygen atmosphere are reported to be 498 m^2/g [12]. Compared to 232 m^2/g achieved with *HT 300 °C 120 min* further indicating that the calcination in the TGA is not suitable.

The pore diameter generated with the BJH method is estimated to be around 4.8-4.9 nm for the samples heated with 300 $°C$ and 4.2 nm for the sample heated with 260 $°C$. The average pore diameter, derived according to Gurvich rule [35], is between 4.1-5.4 nm for the analyzed samples.

The difference between both derived diameters is a result of different assumptions made for the methods. While the BJH method relies on the capillary condensation happening in mesopores the specific BET surface area assumes an adsorbed monolayer on the surface of meso- and micropores. The average diameter derived with the specific BET surface area is thus underestimated. Therefore, the BJH derived pore diameter (Table 6.5) is more trustworthy. Although, due to the open hysteresis loop and the subsequent calculation only from the adsorption branch also this values is of limited relevance.

However, the pore diameter derived with the BJH method for the ex-situ sample, with the highest calcination (*HT 300 °C 120 min*), is about about 4.9 nm, while the pore diameter estimated with the single-step form factor fit of a representable sample is about 5.5 nm.

The higher estimation of the pore diameter for the form factor models is also observed by Jähnert et al. [43]. With all these limitations and results combined it is indicated that it is possible to use the single-step model to estimate the mesopore size with SAXS.

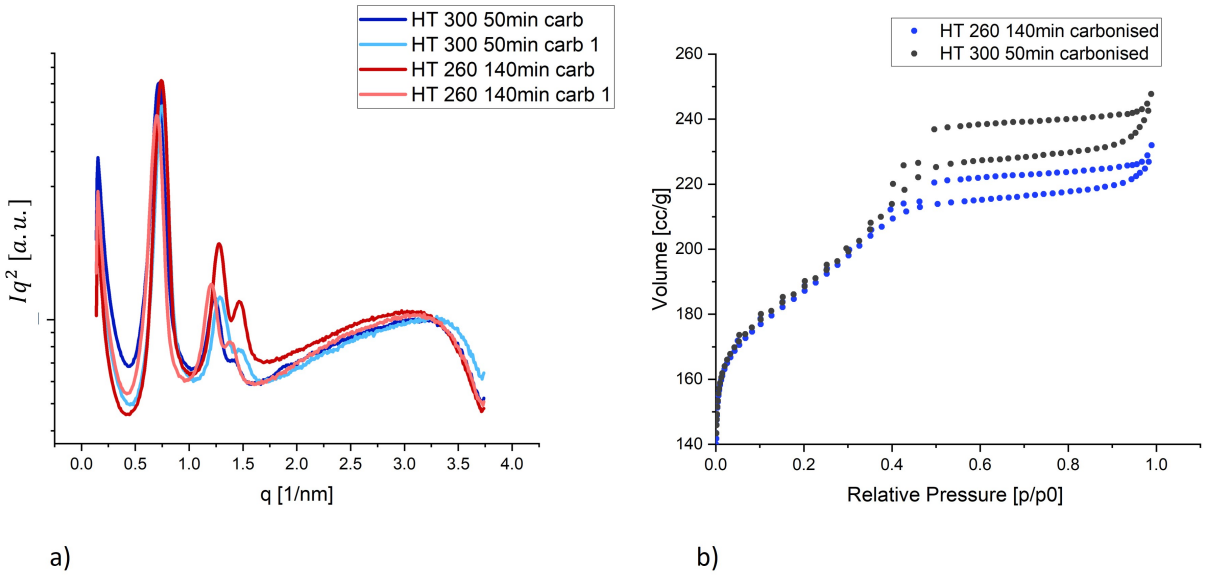

Figure 6.12: a) SAXS profiles and b) gas adsorption isotherms for ex-situ samples carbonized condition

For application purposes, only the carbonized and in most cases additionally activated conditions are relevant. Therefore, samples *HT 260 °C 140 min* and *HT 300 °C 50 min* are carbonized with a heating rate of 1 $°C/min$ up to 850 $°C$ and held for 1 h under Argon atmosphere. The results of the SAXS and gas adsorption measurements are shown in Figure 6.12a). The SAXS data clearly indicates microporosity due to the broad shoulder at high q values. The differences between the SAXS curves are small. This indicates that even though the calcination is incomplete, a large surface area can be generated.

Analyzing the adsorption measurements in Figure 6.12b) the carbonized *HT 300 °C 50 min* sample possesses more mesopores than the other sample.

This further demonstrates that the template is only partially removed in the ex-situ sample *HT 260 °C 140 min* and possibly in *HT 300 °C* as well. The BET area is estimated to be 693 m^2/g for the sample calcinated at 260 $°C$ and for the other one, it is calculated to be 714 m^2/g. Compared to 779 m^2/g achieved by Haswegawa et al. [12] this results look promising. Considering that calcination is not done optimally for the samples in this thesis, these relatively high surface areas are surprising. This indicates that a high surface area can be obtained even though incomplete heat treatment is performed.

6.5 Finding Optimized Parameters

After considering all previous results, this chapter will compare multiple measurements with varying holding temperatures, heating rates and oxygen gas flow. These optimized parameters are done for the setup at ELETTRA with the gas flowing through the sample rather than being exposed to an atmosphere similar to the TGA measurements. To optimize the calcination for such specifications the optimized parameters presented here may need to be altered to suit a different setup. Nevertheless, this work represents a collection of the effects of changing process parameters and hints at how parameters should be chosen.

In Figure 6.13 a comparison of multiple samples heated either under N_2 gas flow with O_2 (purple 2 % oxygen, green 10 % oxygen) provided after reaching HT a) or under oxygen containing gas flow (blue 2 % oxygen, pink 10 % oxygen) from the beginning b) are presented. The relative integrated Bragg intensity is shown with respect to reaching holding temperature, for the samples heated under N_2 gas flow, or to reaching 240 $°C$, for the samples heated under oxygen gas flow. The data indicate that the samples treated with 10 % oxygen reach lower values, meaning their two-dimensional hexagonal structure is not preserved and changes to the structure occur reducing $\tilde{I}_{Bragg}$. This is especially true for the samples constantly experiencing an oxygen gas flow. To check if no false assumptions are made while discussing relative values, Figure 9.2 in the appendix shows the absolute values, which also indicates the same behavior.

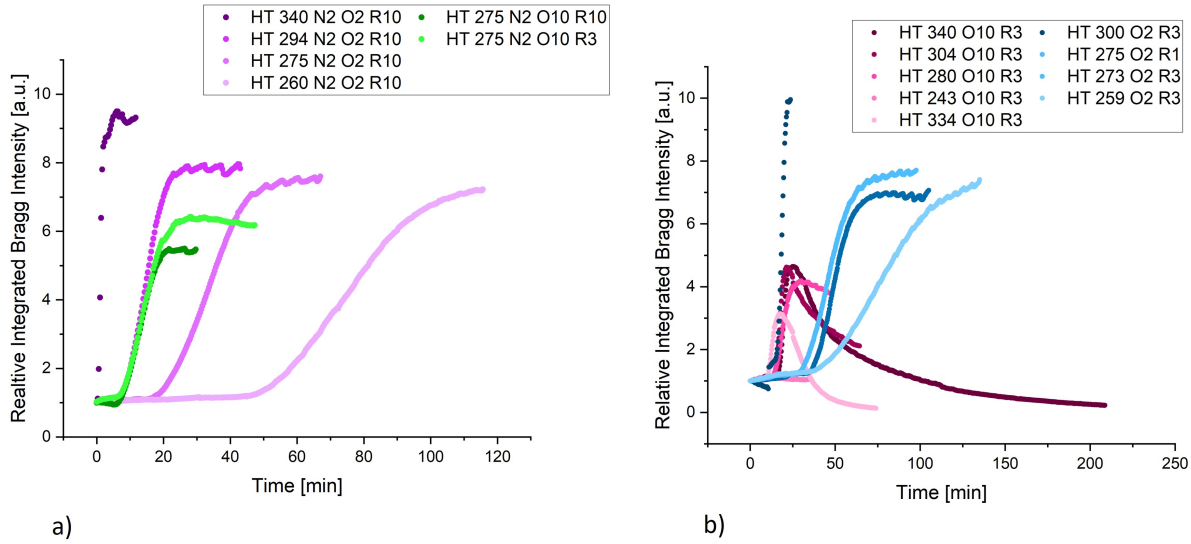

Figure 6.13: a) Comparison of relative $\tilde{I}_{Bragg}$ for in-situ samples heated under pure N_2 atmosphere starting after reaching HT, b) comparison of relative $\tilde{I}_{Bragg}$ for in-situ samples heated under oxygen atmosphere starting after reaching 240 $°C$

Due to the reduction in integrated Bragg intensity and the correlation of this value to the integrity of the two-dimensional hexagonal structure, a lower oxygen content in the atmosphere is preferable. A possible process to describe the loss in structural integrity is later described in this chapter. This conclusion is also suggested by two TGA measurements with the same time and temperature protocol with 2 % and 10 % oxygen atmosphere. For 10 % oxygen atmosphere, the final relative mass is 52.5 % and for 2 % it is 60.7 %.

The structural change according to the SAXS data is much faster and more pronounced for samples treated with 10% oxygen nitrogen ratio. This is also confirmed by the previously presented difference in final mass when comparing 10 % and 2 % oxygen mixtures. The difference in final mass loss is then be explained by the removal of pore walls.

Similar to these described graphs in Figure 6.14, the relative integrated diffuse intensity is depicted with respect to the same characteristic points. These graphs show that the above-described difference in integrated intensity can also be seen, although to a lesser extend, in the diffuse intensity.

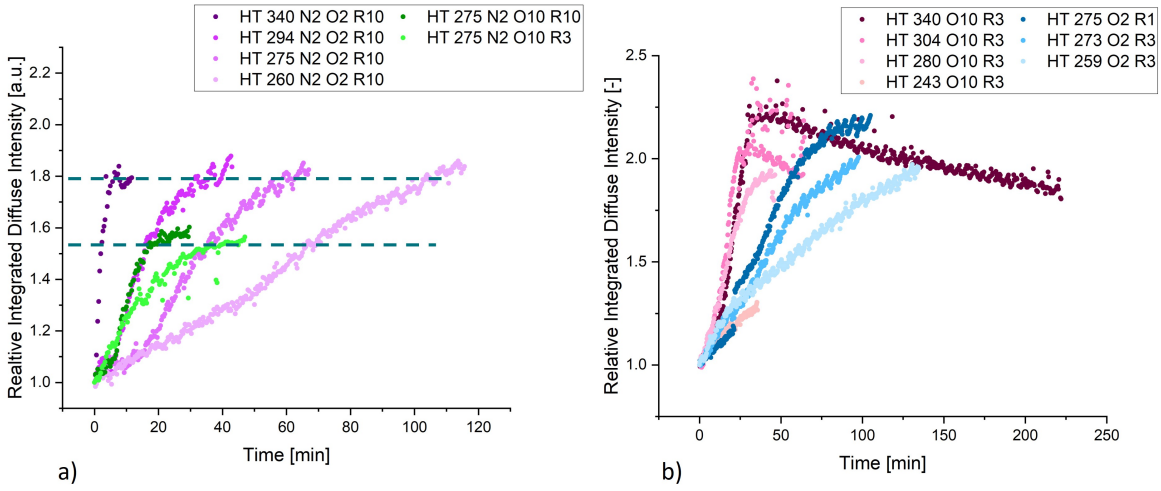

Figure 6.14: a) Comparison of relative $\tilde{I}_{diff}$ from in-situ samples heated under pure N_2 atmosphere starting after reaching HT, b) comparison of relative $\tilde{I}_{diff}$ for in-situ samples heated under oxygen atmosphere starting after reaching $240°C$

The influence of the oxygen nitrogen mixture during calcination is also indicated in the comparison of the power law exponent in Figure 6.15. The decrease in the power law exponent α is less pronounced in the in-situ samples treated with 10 % oxygen containing gas flow compared to the samples treated with 2 % oxygen containing gas flow. This also indicates that the calcination with 10 % oxygen is faster. It can also be seen that the samples treated with 2 % oxygen (with the exception of *HT 340 N2 O2 R10*) reach higher power law values after reaching a minimum value after oxygen injection, while the others reach approximately the same values. This also contributes to the assumption that the removal of pore walls is more pronounced with 10 % oxygen atmosphere.

If the temperature is to high (*HT 340 N2 R1 O2* in Figure 6.15b)), no negative peak for α is visible. This indicates that the reaction happened very fast. Even though the sample is treated under 2 % oxygen the values are closer to the values of the samples treated with 10 % oxygen. This indicates that the structural degradation also occurs at elevated temperatures.

The next parameter to be optimized is the temperature. These graphs (Figures 6.13, 6.14 and 6.15) clearly depict, that with higher holding temperatures the reactions in the sample happen faster. As can be seen in Figure 6.13 the temperature does not influence the integrated Bragg intensity negatively but with lower temperature, the sample must be kept at a holding temperature for a longer period.

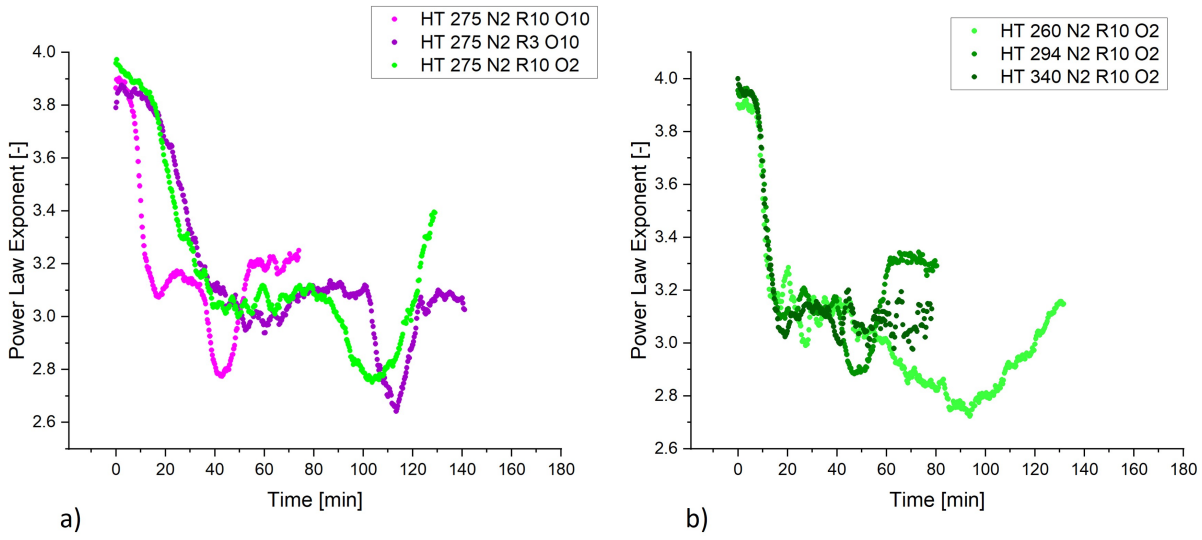

Figure 6.15: Comparison of the power law exponent for the in-situ samples heated to target HT under pure N_2 atmosphere with oxygen injection after reaching HT, each curve is vertically spaced with 0.5 difference between each other

Trying to estimate the effect of the heating rate is difficult with the data generated in this work. Due to a lack of time and some experiments failing, there is no data set with only changing heating rates. In an attempt to hint at the effect of the heating rate, Figure 6.16 shows samples with the same temperature but with different oxygen gas flow, different heating conditions (i.e. heating under N_2 or under oxygen) and with different heating rates. The graph depicts the change in integrated Bragg intensity over the course of the experiment. Depending on the gas flow under heating, the starting point of each curve corresponds to reaching 240 $°C$ (samples heated under oxygen containing gas flow) or to reaching holding temperature (samples heated under nitrogen gas flow). Figure 6.16 shows that the effects of the other parameters are probably greater than the heating rate. It indicates, that heating under N_2 might be good for the integrity of the pore structure. The sample heated under N_2 tends to reach higher integrated Bragg intensity values than their counterparts under constant oxygen gas flow.

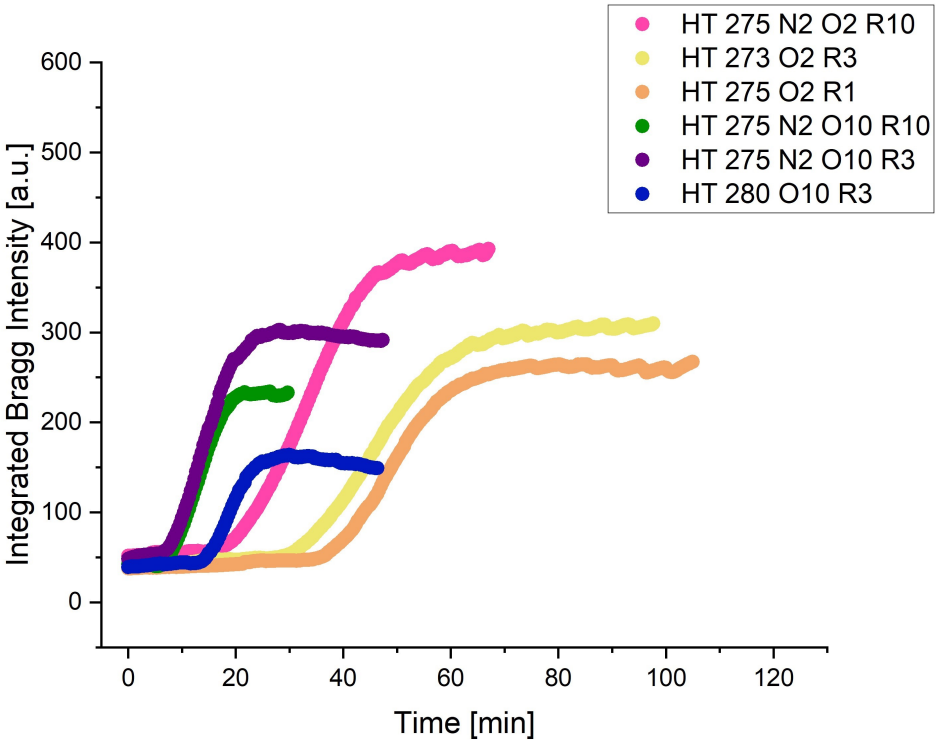

Figure 6.16: Comparison of $\tilde{I}_{Bragg}$ for in-situ samples with similar HT but different heating conditions, oxygen gas flow and heating rates

7 Mistakes and Failed Analytical Steps

This chapter is a summary of some mistakes and failed analytical steps performed during this thesis. One mistake was, that the first few measurements performed at ELETTRA, where done on samples from the outermost region of the monolith rather than from the middle. As mentioned, it was possible to detect heterogeneities in the sample with the naked eye. It was eventually corrected during the time in Trieste but should have been detected earlier. This could have reduced the differences between the samples significantly.

It was assumed, that the samples generated by the in-situ measurements could be analyzed with gas adsorption. The remaining material had to little mass and subsequently not enough surface area for the analysis. Ideally, multiple filled capillaries are placed in the furnace at the same time, under the same conditions, while only one sample is investigated with x-rays. If the in-situ samples could have been investigated straight away, the SAXS data could have been directly compared to the N_2 adsorption isotherms without assumptions.

At the beginning of developing a script for fitting the data, it is assumed that the peak fit could be done without multiple restrictions. This quickly proved to be impossible and some time was spent finding the right restrictions after the code was completed. It would have been better, to look at multiple complete curves and then start fitting the curve with the weakest peaks and test the fitting method on such profiles. Similar issues are discovered during the development of the script and time could have been saved by discovering the main influential fitting parameters at the beginning. The logic of the final fitting described in this thesis may be useful for similar projects and could lead to a faster development of future scripts.

The two-step form factor fit was especially challenging and a lot of time was spent tuning its parameters.

8 Conclusion

In this work the influence of temperature, time, ratio of nitrogen and oxygen in the atmosphere and heating rate on the calcination treatment of STC precursor material are studied. As suggested by the in-situ SAXS data and TGA, long exposure to high temperature can lead to strong structural changes in the material. It is suggested that the walls between the hexagonal arranged pores are partially removed. If this is proven for similar STCs by applying other techniques, it is possible to quantify this effect with SAXS and subsequently provide additional means to tailor the pore structure. For further discussion, an optimal structure refers to a structure with completely removed template while keeping the pore walls intact.

It is indicated that higher oxygen content in the supplied calcination atmosphere enhances the structural changes similar to higher temperatures and longer time. Material treated with 10% oxygen did not reach the same relative integrated Bragg intensities, indicating that the structural decay is far more pronounced, making this condition unsuitable for tailoring the structure. The influence of the heating rate on the structure could not be investigated in depth in the scope of this study. It is assumed that it has little to no effect on the structural integrity. This is promising for industrial applications but additional tests are recommended.

Even though, the gas flow conditions are not studied in this thesis, comparing the indications made by in-situ SAXS analysis with TGA measurements, suggest that the influence cannot be neglected. While samples treated in TGA are not subjected to a direct flow of gas, scattering experiments on STCs were performed with a direct flow of gas through porous solid. The later indicates a much faster and complete calcination. The effects of forced gas flow through the sample should be investigated and could lead to an additional increase in the surface area.

Combining all results for an optimal structure, the oxygen nitrogen mixture should be lower than 10 % O_2. For heat treatments with a forced flow of gas through the material, temperature and time can be varied between 260-300 $°C$, while maintaining enough control over the mesostructure.

The comparison of pore sizes derived with gas adsorption measurements with the model based fit of the SAXS profiles, suggest that the pore size can be estimated with a single-step cylindrical model. This study also provides sufficient information so that future in-situ experiments can be conducted with lab source and longer exposure times. The loss in time resolution can be estimated and evaluated with the information generated in this work.

8.1 Outlook

During this thesis it was not possible to produce and measure calcinated samples with gas adsorption in the same (apparent) conditions as indicated by in-situ measurements. As described, the ex-situ samples prepared in the TGA were not heat treated similar to the in-situ experiments due to the different gas flow conditions. It was not possible to gain access to a furnace where the atmosphere can similarly be changed to the in-situ experiments, while also having comparable gas flow conditions. Resolving this issue and producing samples that can be directly correlated to the in-situ SAXS data could further enhance the assumptions made in this work.

The conclusions made in this work are promising for further applications and could lead to an increase in performance of certain devices. This also needs to be investigated and experiments need to be conducted to evaluate the influence of the calcination on the final performance of devices (e.g supercapacitors).

As the gas flow conditions during calcination are indicated to play a non negligible role, experiments should be conducted to confirm some of the assumptions made in this thesis. Different, more sophisticated models could be used to describe the structural changes during calcination. The models used in the work of Förster et al. [34] and Losito et al. [44], that were applied on mesoporous silica, could be adapted to STCs. If successful, this could lead to a better fit for the existing data and possibly the whole heat treatment can be fitted with two steps or even gradients can be introduced instead of steps. In addition to trying out different models the fit of the model described in this work can also be adapted to increase the quality of the fit. If for example the fit chooses a parameter set that changed a lot compared to the previous fit while reducing the quality of the fit, the fitting values should be manually adapted so that the fit can continue with reasonable values. Both could lead to an improved form factor fit and could allow for more assumptions of the structural changes during calcination. It is unclear what causes the color difference in Figure 4.3 a) and what impact this might have on the micro- and mesostructure. This should further be investigated with SAXS and TEM, in order to estimate the structural differences in one sample.

References

1. Simon, P. & Gogotsi, Y. Materials for electrochemical capacitors. *Nature materials* **7,** 845–854 (2008).
2. Koczwara, C. *et al.* Nanofibers versus Nanopores: a comparison of the electrochemical performance of hierarchically ordered porous carbons. *ACS Applied Energy Materials* **2,** 5279–5291 (2019).
3. Koczwara, C. *Performance evaluation and in situ X-ray scattering of ordered mesoporous carbons for electrochemical energy storage applications* PhD thesis (Montanuniversitaet Leoben, 2019). `https://pure.unileoben.ac.at/portal/files/4335115/AC15512625n01.pdf`.
4. Kostoglou, N. *et al.* Nanoporous activated carbon cloth as a versatile material for hydrogen adsorption, selective gas separation and electrochemical energy storage. *Nano Energy* **40,** 49–64 (2017).
5. Krüner, B. *et al.* Hydrogen-treated, sub-micrometer carbon beads for fast capacitive deionization with high performance stability. *Carbon* **117,** 46–54 (2017).
6. Porada, S., Zhao, R., Van Der Wal, A., Presser, V. & Biesheuvel, P. Review on the science and technology of water desalination by capacitive deionization. *Progress in materials science* **58,** 1388–1442 (2013).
7. Shao, H., Wu, Y.-C., Lin, Z., Taberna, P.-L. & Simon, P. Nanoporous carbon for electrochemical capacitive energy storage. *Chemical Society Reviews* **49,** 3005–3039 (2020).
8. Zhong, C. *et al.* A review of electrolyte materials and compositions for electrochemical supercapacitors. *Chemical Society Reviews* **44,** 7484–7539 (2015).
9. Breitsprecher, K., Holm, C. & Kondrat, S. Charge me slowly, I am in a hurry: Optimizing charge–discharge cycles in nanoporous supercapacitors. *ACS nano* **12,** 9733–9741 (2018).
10. Momčilović, M. *et al.* Complex electrochemical investigation of ordered mesoporous carbon synthesized by soft-templating method: charge storage and electrocatalytical or Pt-electrocatalyst supporting behavior. *Electrochimica Acta* **125,** 606–614 (2014).

11. Putz, F., Ludescher, L., Elsaesser, M. S., Paris, O. & HuÌˆsing, N. Hierarchically organized and anisotropic porous carbon monoliths. *Chemistry of Materials* **32,** 3944–3951 (2020).

12. Hasegawa, G. *et al.* Hierarchically porous carbon monoliths comprising ordered mesoporous nanorod assemblies for high-voltage aqueous supercapacitors. *Chemistry of Materials* **28,** 3944–3950 (2016).

13. Day, G., Drake, H., Zhou, H. & Ryder, M. Evolution of porous materials from ancient remedies to modern frameworks. *Communications Chemistry* **4,** 1–4 (2021).

14. Sonu, K., Laha, S., Eswaramoorthy, M. & Maji, T. Porous Materials: Recent Developments. *Advances in the Chemistry and Physics of Materials: Overview of Selected Topics,* 148–172 (2020).

15. Rouquerol, J. *et al.* Recommendations for the characterization of porous solids (Technical Report). *Pure and applied chemistry* **66,** 1739–1758 (1994).

16. Van Der Voort, P., Leus, K. & De Canck, E. *Introduction to Porous Materials* (John Wiley & Sons, 2019).

17. Chowdhury, A. H., Salam, N., Debnath, R., Islam, S. M. & Saha, T. in *Nanomaterials Synthesis* 265–294 (Elsevier, 2019).

18. Bruce, D., O'Hare, D. & Walton, R. *Porous materials* (John Wiley & Sons, 2011).

19. Liu, P. & Chen, G. *Porous materials: processing and applications* (Elsevier, 2014).

20. Marsh, H. & Reinoso, F. *Activated carbon* (Elsevier, 2006).

21. Wang, R., Zheng, S. & Zheng, Y. *Polymer matrix composites and technology* (Elsevier, 2011).

22. Frackowiak, E., Machnikowski, J. & Béguin, F. in *New Carbon Based Materials for Electrochemical Energy Storage Systems: Batteries, Supercapacitors and Fuel Cells* 5–20 (Springer, 2006).

23. Jérôme, F. & Valange, S. Rational Design of Nanostructured Carbon Materials: Contribution to Cellulose Processing. *Nanotechnology in Catalysis: Applications in the Chemical Industry, Energy Development, and Environment Protection,* 627–654 (2017).

24. Schnablegger, H. & Singh, Y. *The SAXS guide: getting acquainted with the principles* 1–124 (Anton Paar: Graz, Austria, 2011).

25. Pecharsky, V. & Zavalij, P. *Fundamentals of Powder Diffraction and Structural Characterization of Materials, Second Edition* (Springer, 2009).

26. Melnichenko, Y. *Small-Angle Scattering from Confined and Interfacial Fluids* (Springer, 2016).

27. Wess, T. *et al.* The use of small-angle X-ray diffraction studies for the analysis of structural features in archaeological samples. *Archaeometry* **43,** 117–129 (2001).

28. Zickler, G. *et al.* Physisorbed films in periodic mesoporous silica studied by in situ synchrotron small-angle diffraction. *Physical Review B* **73,** 184109 (2006).

29. Findenegg, G., Jähnert, S., Müter, D. & Paris, O. Analysis of pore structure and gas adsorption in periodic mesoporous solids by in situ small-angle X-ray scattering. *Colloids and Surfaces A: Physicochemical and Engineering Aspects* **357,** 3–10 (2010).

30. Glatter, O. *Scattering methods and their application in colloid and interface science* (Elsevier, 2018).

31. Porod, G. Die Röntgenkleinwinkelstreuung von dichtgepackten kolloiden Systemen. *Kolloid-Zeitschrift* **124,** 83–114 (1951).

32. Imperor-Clerc, M., Davidson, P. & Davidson, A. Existence of a microporous corona around the mesopores of silica-based SBA-15 materials templated by triblock copolymers. *Journal of the American Chemical Society* **122,** 11925–11933 (2000).

33. Pedersen, J. Analysis of small-angle scattering data from colloids and polymer solutions: modeling and least-squares fitting. *Advances in colloid and interface science* **70,** 171–210 (1997).

34. Förster, S. *et al.* Scattering curves of ordered mesoscopic materials. *The Journal of Physical Chemistry B* **109,** 1347–1360 (2005).

35. Lowell, S., Shields, J. E., Thomas, M. A. & Thommes, M. *Characterization of porous solids and powders: surface area, pore size and density* (Springer Science & Business Media, 2006).

36. Bardestani, R., Patience, G. & Kaliaguine, S. Experimental methods in chemical engineering: specific surface area and pore size distribution measurementsBET, BJH, and DFT. *The Canadian Journal of Chemical Engineering* **97,** 2781–2791 (2019).

37. Newville, M. *et al. Lmfit: Non-Linear Least-Square Minimization and Curve-Fitting for Python* Astrophysics Source Code Library, record ascl:1606.014. 2016.

38. Virtanen, P. *et al.* SciPy 1.0: Fundamental Algorithms for Scientific Computing in Python. *Nature Methods* **17,** 261–272 (2020).

39. Bérubé, F. & Kaliaguine, S. Calcination and thermal degradation mechanisms of triblock copolymer template in SBA-15 materials. *Microporous and mesoporous materials* **115,** 469–479 (2008).

40. Sienkiewicz, A., Krasucka, P., Charmas, B., Stefaniak, W. & Goworek, J. Swelling effects in cross-linked polymers by thermogravimetry. *Journal of Thermal Analysis and Calorimetry* **130,** 85–93 (2017).

41. Weber, J., Antonietti, M. & Thomas, A. Microporous networks of high-performance polymers: Elastic deformations and gas sorption properties. *Macromolecules* **41,** 2880–2885 (2008).

42. Florek, J., Guillet-Nicolas, R. & Kleitz, F. in *Functional Materials* 61–100 (De Gruyter, 2014).

43. Jähnert, S. *et al.* Pore structure and fluid sorption in ordered mesoporous silica. I. Experimental study by in situ small-angle x-ray scattering. *The Journal of Physical Chemistry C* **113,** 15201–15210 (2009).

44. Losito, D. *et al.* Mesoporous Silica–Fe3O4 Nanoparticle Composites as Potential Drug Carriers. *ACS Applied Nano Materials* **4,** 13363–13378 (2021).

9 Appendix

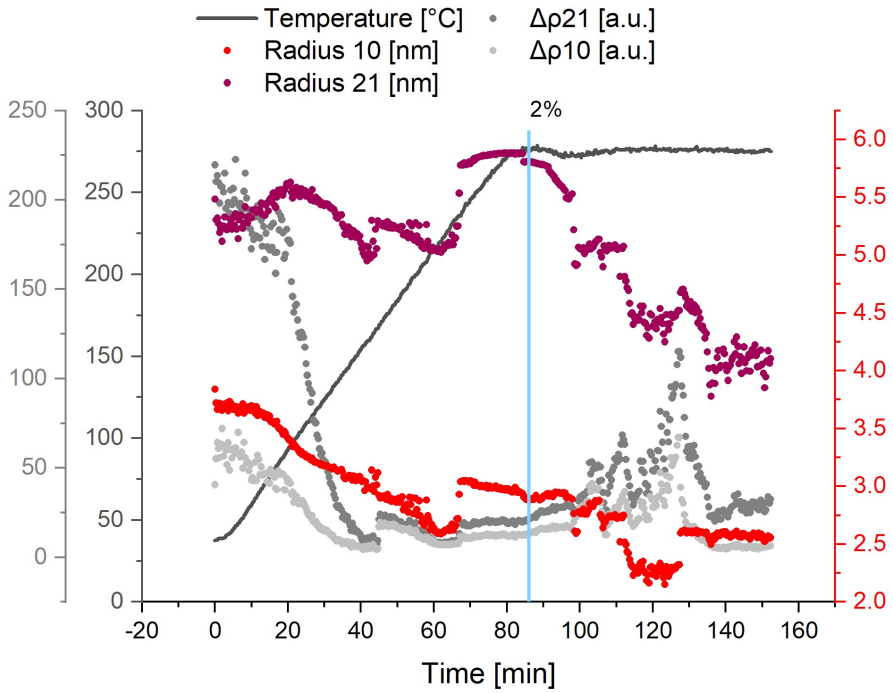

Figure 9.1: Results from two-step form factor model fitted for in-situ sample *HT 275 N2 O2 R3*

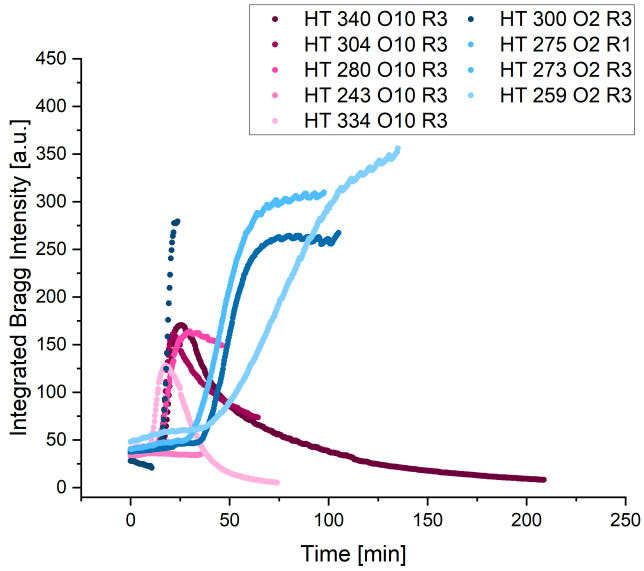

Figure 9.2: Comparison of $\tilde{I}_{Bragg}$ for samples heated under oxygen gas flow

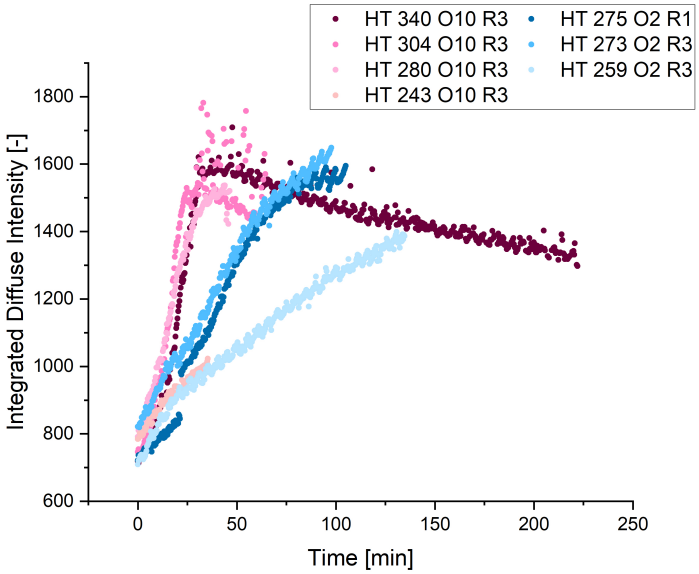

Figure 9.3: Comparison of $\tilde{I}_{diff}$ for samples heated under oxygen gas flow

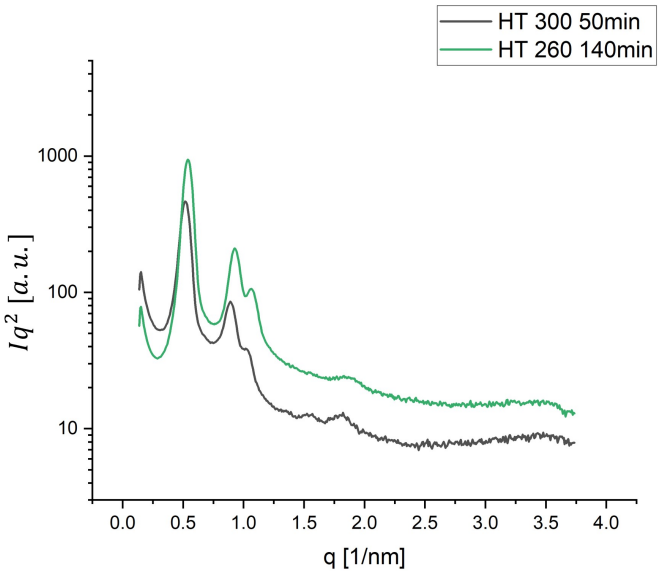

Figure 9.4: SAXS profiles of ex-situ samples in calcinated condition

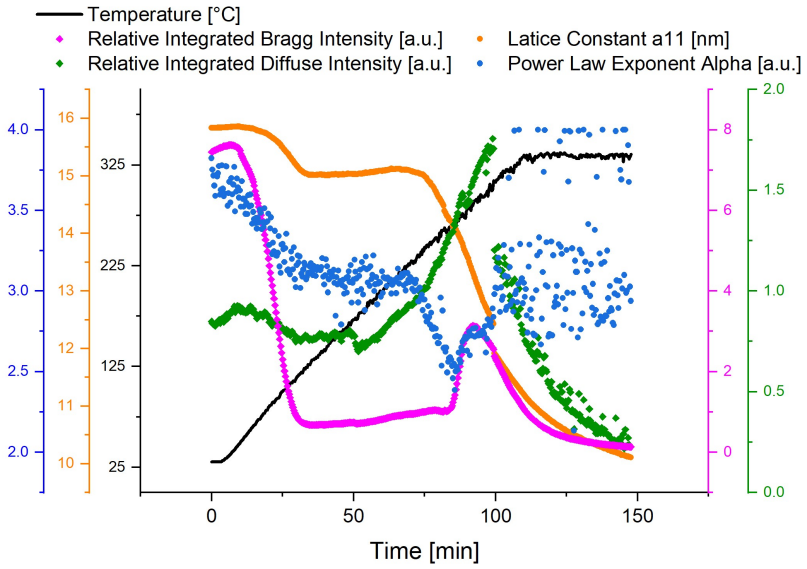

Figure 9.5: Mutliaxial plot for in-situ sample *HT 334 O10 R3*

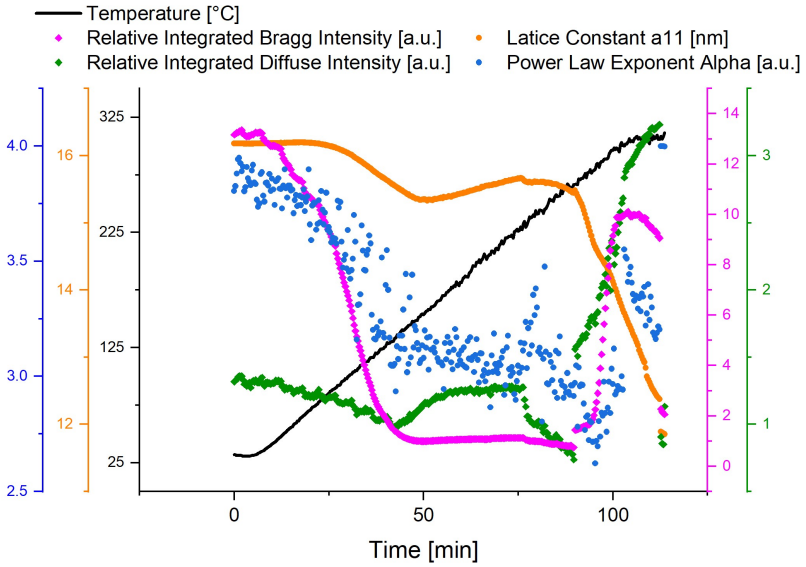

Figure 9.6: Mutliaxial plot for in-situ sample *HT 300 O2 R3*

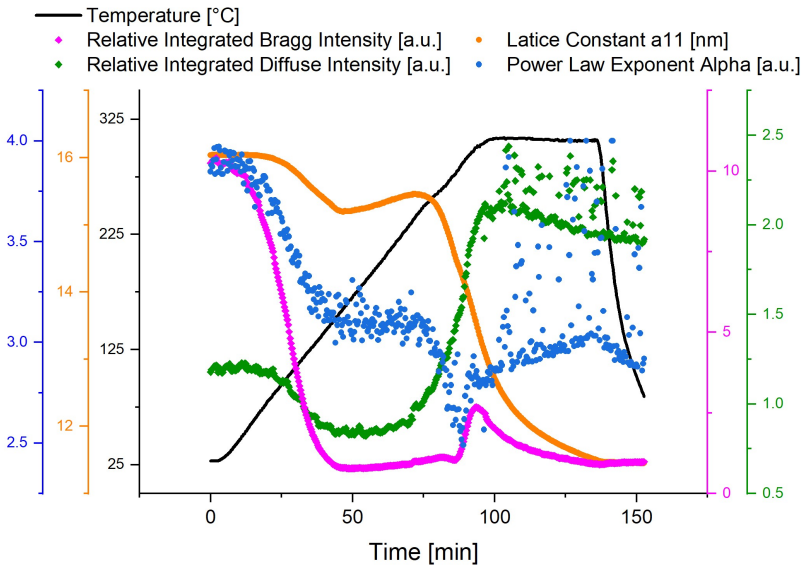

Figure 9.7: Mutliaxial plot for in-situ sample *HT 304 O10 R3*

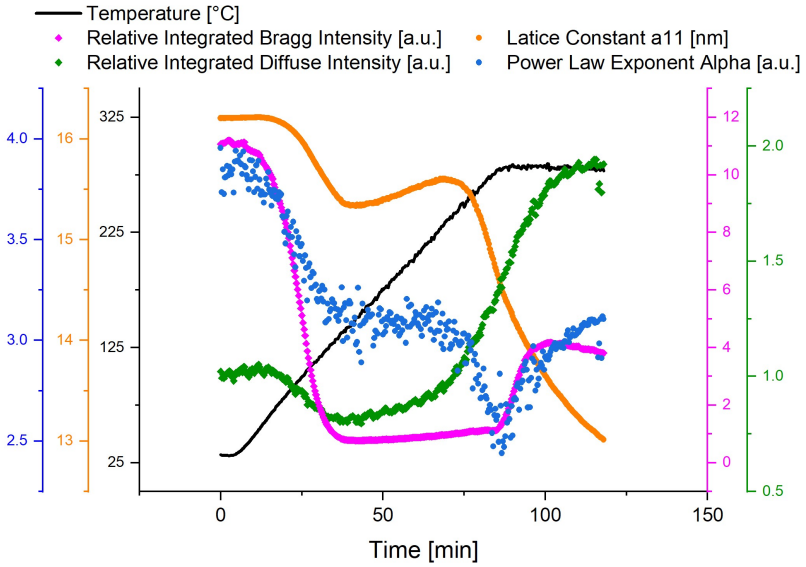

Figure 9.8: Mutliaxial plot for in-situ sample *HT 280 O10 R3*

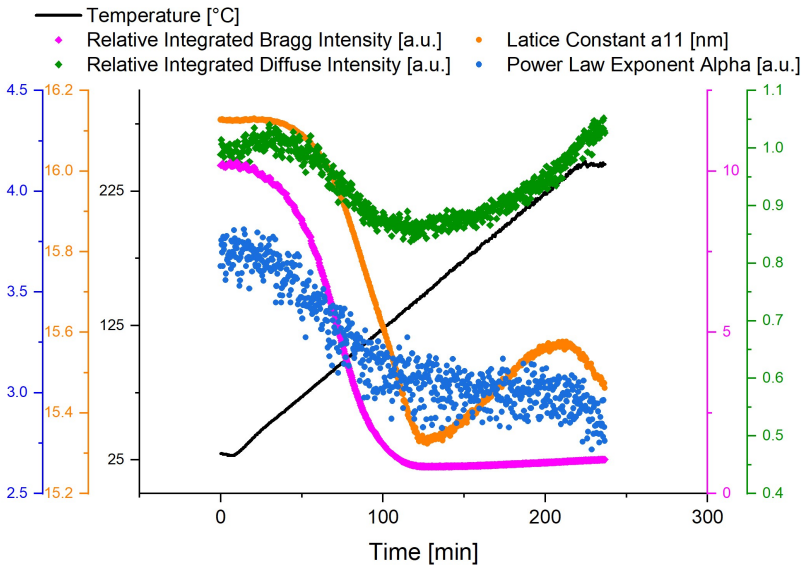

Figure 9.9: Mutliaxial plot for in-situ sample *HT 245 O2 R1*

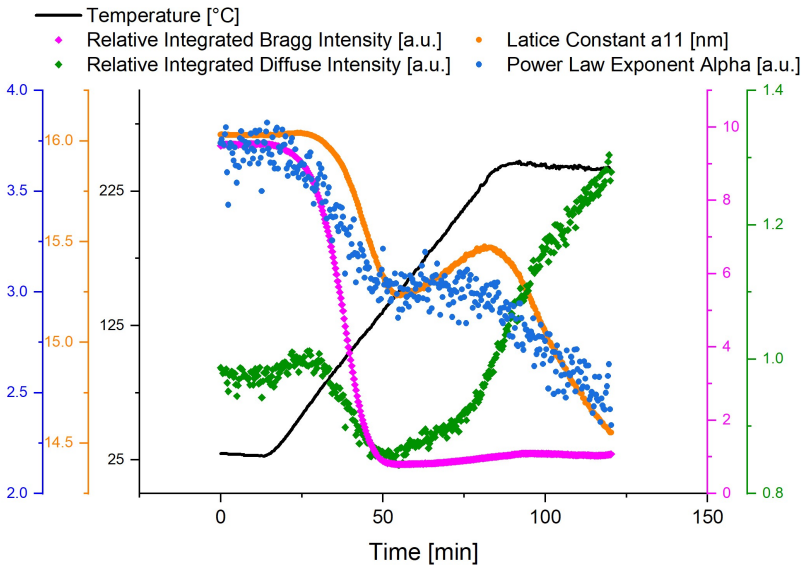

Figure 9.10: Mutliaxial plot for in-situ sample *HT 243 O10 R3*

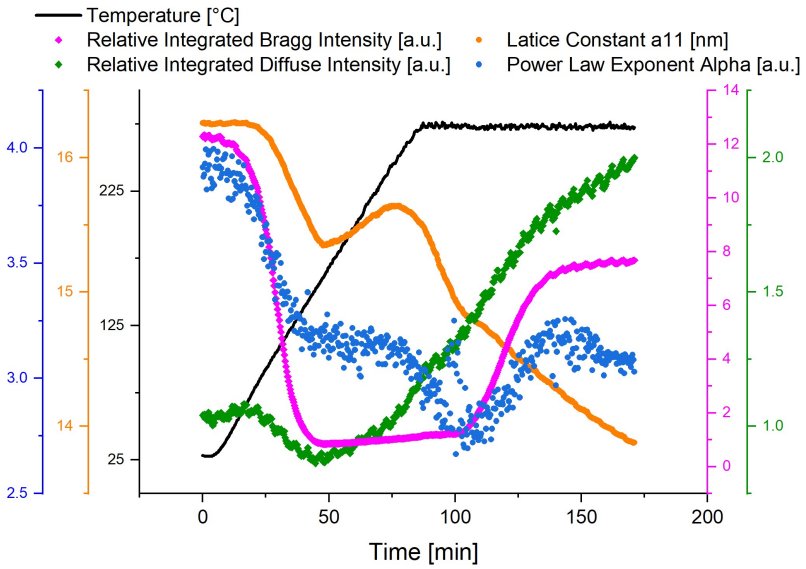

Figure 9.11: Mutliaxial plot for in-situ sample *HT 273 O2 R3*

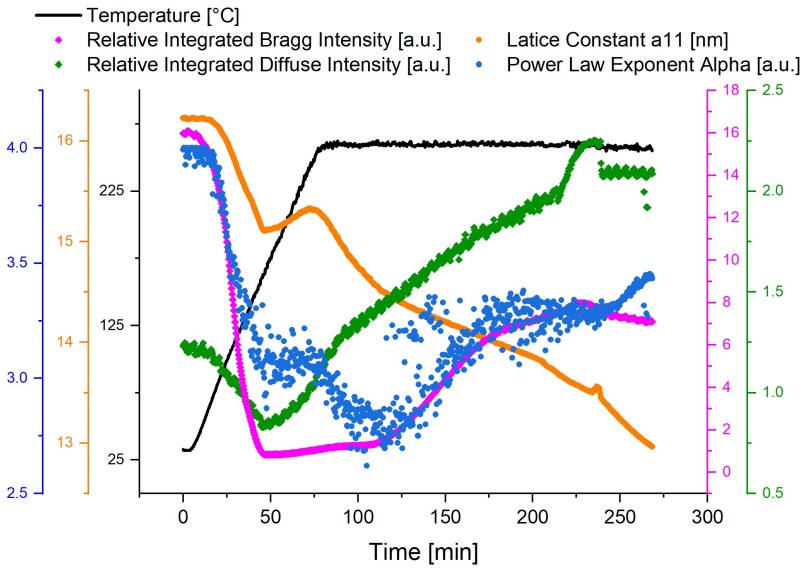

Figure 9.12: Mutliaxial plot for in-situ sample *HT 259 O2 R3*

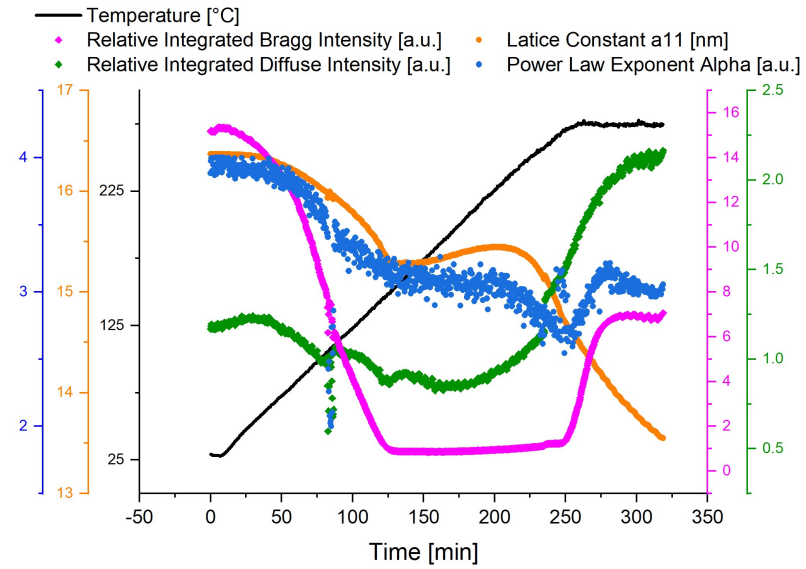

Figure 9.13: Mutliaxial plot for in-situ sample *HT 275 O2 R1*

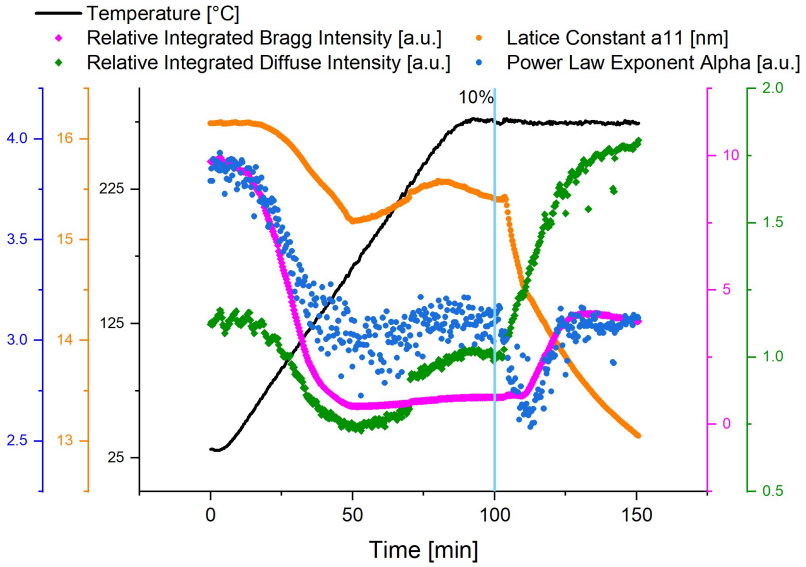

Figure 9.14: Mutliaxial plot for in-situ sample *HT 300 N2 O2 R10*

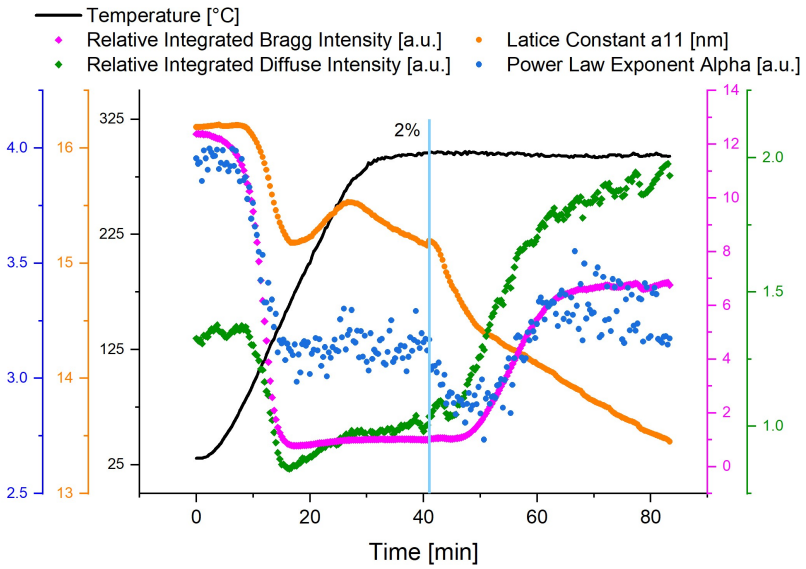

Figure 9.15: Mutliaxial plot for in-situ sample *HT 294 N2 O2 R10*

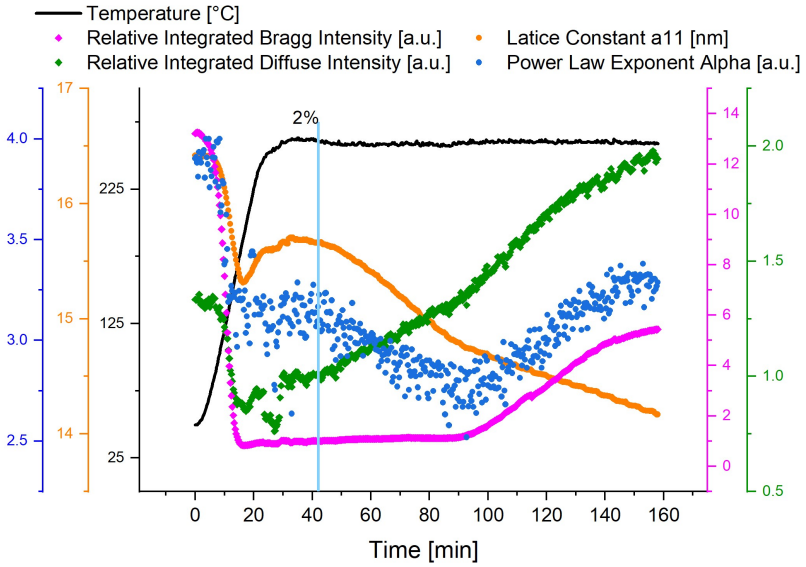

Figure 9.16: Mutliaxial plot for in-situ sample *HT 260 N2 O2 R10*

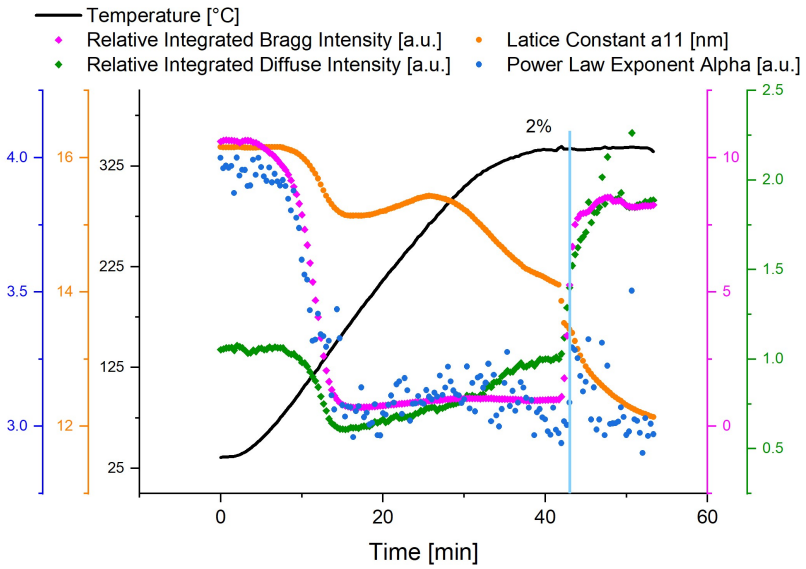

Figure 9.17: Mutliaxial plot for in-situ sample *HT 340 N2 O2 R10*

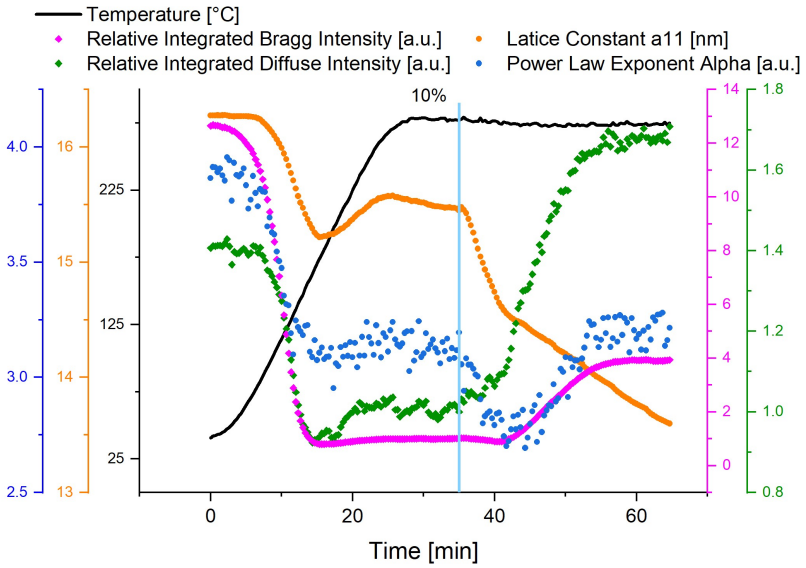

Figure 9.18: Mutliaxial plot for in-situ sample *HT 274 N2 O10 R10*